

# The Multi-phase Absorption Systems Toward PG 1206+459<sup>1,2,3</sup>

Jie Ding, Jane C. Charlton<sup>4</sup>, Christopher W. Churchill<sup>5,6</sup>, and Christopher Palma

*Department of Astronomy and Astrophysics  
The Pennsylvania State University  
University Park, PA 16802  
ding, charlton, cwc, cpalma@astro.psu.edu*

*The Pennsylvania State University, University Park, PA 16802*

## ABSTRACT

A high-resolution ( $R = 30,000$ ) ultraviolet spectrum is presented, which covers Ly $\alpha$  and many low-, intermediate-, and high-ionization transitions in the three MgII-selected absorption systems toward the quasar PG 1206+459. Three systems (A, B, and C), which are clustered within  $1500 \text{ km s}^{-1}$  at  $z \sim 0.93$ , were originally identified in a spectrum obtained with the High Resolution Spectrograph (HIRES) on the Keck I telescope. A WIYN Gunn  $i$ -band image of the quasar field and spectroscopy of two galaxy candidates are presented. A multi-phase medium is seen in all three systems, consistent with smaller, denser clouds producing low-ionization transitions (MgII, FeII, and SiII) and larger, diffuse, photoionized clouds giving rise to higher-ionization transitions (CIV, NV,

---

<sup>1</sup>Based in part on observations obtained at the W. M. Keck Observatory, which is operated as a scientific partnership among Caltech, the University of California, and NASA. The Observatory was made possible by the generous financial support of the W. M. Keck Foundation.

<sup>2</sup>Based in part on observations obtained with the NASA/ESA *Hubble Space Telescope*, which is operated by the STScI for the Association of Universities for Research in Astronomy, Inc., under NASA contract NAS5-26555.

<sup>3</sup>Based in part on observations obtained with the WIYN 3.5-m telescope, a joint facility of the University of Wisconsin-Madison, Indiana University, Yale University, and the National Optical Astronomy Observatories.

<sup>4</sup>Center for Gravitational Physics and Geometry

<sup>5</sup>Visiting Astronomer at the W. M. Keck Observatory

<sup>6</sup>Visiting Astronomer, Kitt Peak National Observatory, National Optical Astronomy Observatory, which is operated by the Association of Universities for Research in Astronomy, Inc. (AURA) under cooperative agreement with the National Science Foundation.

and/or OVI). (1) System A, a multi-cloud, weak MgII absorber at  $z = 0.9254$ , requires a super-solar metallicity in both low- and high-ionization phases, unless an  $\alpha$ -group enhancement is included. The low-ionization absorption is produced in clouds with sizes of 10–70 pc, which are surrounded in velocity space by broader, high-ionization components. With the unusually complex velocity structure resolved in the NV profiles, this system is unlikely to represent a traditional galaxy disk/corona. The most likely candidate host galaxy is a  $\sim 2L^*$ , apparently warped, spiral at an impact parameter of  $43h^{-1}$  kpc. (2) System B, at  $z = 0.9276$ , has the strongest MgII absorption and has an approximately solar metallicity in the low-ionization phase. The smooth, broad high-ionization profiles may indicate a coronal structure similar to that of the Milky Way. The redshift of an  $L^*$  galaxy ( $z = 0.9289$ ), at an impact parameter of  $38h^{-1}$  kpc is consistent with the redshift of this system. (3) System C, at  $z = 0.9342$ , has a single component in MgII, separated from the other two systems by  $\sim +1000$  km s $^{-1}$ . The Ly $\alpha$  profile is not aligned with the MgII, requiring an additional velocity component offset by  $-40$  km s $^{-1}$ . System C lacks the small, low-ionization cloud characteristic of an isolated single-cloud, weak MgII absorber. Its absorption properties are similar to the “satellite clouds” of classic strong MgII absorbers, so this could be a high-velocity cloud in the galaxy group responsible for the systems, possibly related to a  $0.2L^*$  galaxy at an impact parameter of  $43h^{-1}$  kpc.

*Subject headings:* quasars— absorption lines; galaxies— evolution; galaxies— halos

## 1. Introduction

Quasar absorption line systems, selected by MgII absorption, sample different types of galaxies with absorption produced by some combination of disk interstellar medium, coronal gas, and high-velocity clouds (Charlton & Churchill 1996, 1998; Steidel et al. 2002). The high-resolution spectra covering multiple chemical transitions reveal detailed information of the kinematic, chemical, and ionization conditions in the different phases of gas along the line of sight. At  $z \sim 1$ , when the universe was roughly half its present age, it is of particular interest to use this information for probing galactic evolution.

Strong MgII systems [ $W_r(2796) > 0.3 \text{ \AA}$ ] at  $0.3 \lesssim z \lesssim 1$  are almost always found within  $\sim 40h^{-1}$  kpc of luminous galaxies (those with luminosities greater than  $0.05L^*$ ) (Bergeron & Boissé 1991; Bergeron et al. 1992; Le Brun et al. 1993; Steidel, Dickinson, & Persson 1994; Steidel 1995; Churchill, Steidel, & Vogt 1996; Steidel et al. 1997). Therefore they provide

excellent probes of the gaseous content in galaxies at intermediate redshifts.

Strong MgII absorbers with twice the typical MgII, FeII, CIV, and Ly $\alpha$  absorption have been classified as “double” systems (Churchill et al. 2000b). These double systems also have twice the typical kinematic spread in their low-ionization components. They could be produced by lines of sight that pass through pairs of galaxies (see Churchill et al. 2000b), though at least one example exists (the double system at  $z = 0.8519$  toward Q 0002 + 052) where only one galaxy has been identified as the absorbing galaxy (Churchill, Steidel, & Vogt 1996). This galaxy has a very blue rest-frame color and a *Hubble Space Telescope* (*HST*) / Wide Field and Planetary Camera (WFPC2) image reveals it to be morphologically compact and apparently isolated (Steidel 1998). These properties are suggestive of an elevated star formation rate. Another interpretation, then, is that the double systems could arise from material mechanically stirred up by star formation processes (Churchill et al. 1999).

A particularly interesting example of the class of double, strong MgII absorbers is found at  $z \sim 0.93$  along the line of sight toward the quasar PG 1206+459 ( $z_{em} = 1.16$ ). Based upon spectra obtained with the High Resolution Spectrograph (HIRES; Vogt et al. (1994)) on Keck I, three separate “groupings” of low-ionization clouds were identified (labeled systems A, B, and C at redshifts  $z = 0.9254, 0.9276,$  and  $0.9343,$  respectively; Churchill & Charlton 1999). Systems A and B were together classified as a double MgII system (Churchill et al. 2000b), whereas system C was classified as a “weak system” (Churchill et al. 1999, 2000b). The low-resolution spectrum of PG 1206 + 459, obtained with the *HST* / Faint Object Spectrograph (FOS), is unusually rich, with strong absorption in the high-ionization transitions (Jannuzi et al. 1998). Churchill & Charlton (1999) studied the *HST*/FOS and the HIRES/Keck spectra and, based upon photoionization modeling of the data, inferred multiple ionization phases in all three systems. The low-ionization “MgII clouds” appear to be embedded in extended, high-ionization, lower density gas that gives rise to the bulk of the CIV, NV, and OVI absorption.

However, since in the previous study only low-resolution profiles were available for many of the key transitions, the kinematic relationships between the low- and high-ionization gas remains unknown. The high-ionization profiles (CIV, NV, and OVI) are resolved in the FOS spectrum ( $\text{FWHM} \simeq 230 \text{ km s}^{-1}$ ), indicating a large velocity spread; however, it could not be determined whether the profiles are smooth (suggesting a monolithic turbulent medium), or are structured (suggesting smaller discrete high-ionization clouds).

As such, a study of this system holds the promise of revealing the comparative nature of the low- and high-ionization gas in a  $z \simeq 1$  galaxy (or small group of galaxies). To better understand the nature of this system, we obtained an  $R = 30,000$  E230M spectrum from the Space Telescope Imaging Spectrograph (STIS) on-board *HST*. This spectrum provided

high-resolution ( $\text{FWHM} \simeq 15 \text{ km s}^{-1}$ ) absorption profiles for the  $\text{Ly}\alpha$ ,  $\text{Si II}$ ,  $\text{C II}$ ,  $\text{Si III}$ ,  $\text{Si IV}$ ,  $\text{C IV}$  and  $\text{N V}$  transitions documented in the FOS spectrum.

Churchill & Charlton (1999) discussed the possibility that the absorption may arise in a small group of galaxies. They tentatively reported a slight over density of galaxies in a ground-based image (Kirhakos et al. 1994) of the QSO field (they identified three bright galaxies within  $5''$  of the QSO). The extreme absorption in systems A + B, their proximity in velocity, and the presence of a weak  $\text{Mg II}$  system  $\sim 1000 \text{ km s}^{-1}$  to the red, make the relationship between the absorption and galaxies all the more tantalizing. There are no other clear galaxy candidates for  $\text{Mg II}$  absorption to arise in such a potentially complex environment. Do the absorption-galaxy relationships suggest that the gaseous structures are coupled to galaxies or dispersed throughout a small-group environment?

To address the absorption-galaxy relationship in this remarkable multiple absorption line system, we obtained a WIYN 3.5-m telescope Gunn  $i$ -band image of the QSO field ( $0.8''$  seeing). We also obtained spectra of the bright galaxies reported by Kirhakos et al. (1994) using the CryoCam Spectrograph on the 4-m telescope at Kitt Peak National Observatory (KPNO). We found that one of the galaxy candidates identified by Kirhakos et al. (1994) did not exist. We successfully obtained the redshift of one of the other galaxies.

In this paper, we present the high-resolution profiles of the absorption arising in systems A, B, and C. We also present a WIYN image of the QSO field. Because not all useful transitions (i.e. higher order hydrogen lines and  $\text{O VI } \lambda\lambda 1032, 1038$ ) were observed at high resolution, we also include the FOS spectrum. We pursue photoionization and collisional ionization modeling of the various ionic transitions measured in both the STIS and HIRES spectra. We derive constraints on the metallicities, abundance patterns, and ionization states of absorbing clouds in the different phases of gas.

In § 2 we briefly describe the Keck/HIRES, *HST*/FOS, and *HST*/STIS spectra that we use to constrain our models. Our WIYN image of the quasar field is presented in § 4, where we discuss our effort to spectroscopically identify host galaxies of the three absorption systems. A summary of our photoionization/collisional ionization modeling techniques is presented in § 5 and the results of our modeling are outlined in § 6. Finally, in § 7, we summarize and consider physical interpretations of the three systems.

## 2. The Data

### 2.1. Keck/HIRES QSO Spectroscopy

The optical spectrum from HIRES (Vogt et al. 1994) extends from 3723 to 6186 Å, and covers the MgII  $\lambda\lambda$ 2796, 2803 doublet, and the MgI  $\lambda$ 2853, FeII  $\lambda$ 2344, 2374, 2383, 2587, and 2600 transitions at  $z = 0.93$ . The spectral resolution is  $R = 45,000$  (FWHM  $\sim 6.6$  km s<sup>-1</sup>) and the signal-to-noise ratio is  $\sim 50$  per three-pixel resolution element (Churchill & Charlton 1999; Churchill & Vogt 2001). The HIRES spectrum was reduced in the standard fashion using IRAF<sup>7</sup>, as described in Churchill & Vogt (2001). The wavelength calibration was vacuum with a heliocentric correction applied.

### 2.2. HST/STIS QSO Spectroscopy

A 24,000 second *HST*/STIS spectrum of PG 1206 + 459 was obtained with the E230M grating in May 2001. E230M covers 2270 Å to 3120 Å. The resulting signal-to-noise ratio ranges from  $5 \lesssim \text{S/N} \lesssim 15$ , and the resolution is  $R = 30,000$  (FWHM  $\sim 10$  km s<sup>-1</sup>). The total exposure time was 24,000 seconds. We reduced the STIS spectrum with the standard pipeline (Brown et al. 2002). The continuum fitting was performed on the extracted spectrum using standard methods (Churchill & Vogt 2001). Absorption lines were detected using the formalism of Schneider et al. (1993) and Churchill et al. (2000a).

### 2.3. HST/FOS QSO Spectroscopy

Even with the availability of high-resolution STIS data, the FOS spectrum is still critical in coverage of some key transitions that are not within the STIS wavelength range. This includes OVI  $\lambda\lambda$ 1032, 1038 as well as the Lyman series and a partial Lyman limit break at 1760 Å. The *HST*/FOS spectra (Jannuzi et al. 1998) covered 1600 Å to 3280 Å using the G190H and G270H gratings, respectively, and had a resolution of  $R = 1,300$  (FWHM  $\sim 230$  km s<sup>-1</sup>). The data reduction, wavelength calibration, and continuum fitting were performed as part of the QSO Absorption Line Key Project (Bahcall et al. 1993, 1996; Jannuzi et al. 1998).

---

<sup>7</sup>IRAF is distributed by the National Optical Astronomy Observatories, which are operated by AURA, Inc., under cooperative agreement with the NSF.

## 2.4. WIYN Imaging

The field surrounding PG 1206 + 459 was observed on 9 February 1999 with the WIYN 3.5-m telescope. The detector (the 2048×2048 CCD imager) provided a  $6'7 \times 6'7$  field of view. The total exposure time of 5840 seconds was divided into 17 dithered images with integration times of 300, 340, and 400 seconds. All observations were taken through a Gunn-*i* filter. The seeing was approximately  $0.8''$ . The raw images were processed using the IRAF package CCDRED.

Aperture photometry of several objects near the quasar was performed using the IRAF APPHOT package. An aperture of radius nine pixels (approximately twice the FWHM of a star) was used to measure the object flux; while the sky was determined by taking the centroid of the pixel values inside an annulus with inner radius ten pixels and outer radius 15 pixels. It is likely that some light from the quasar has affected the estimate of the sky flux, however, we calculated only relative photometry for objects that are approximately equidistant from the center of the QSO, therefore any systematic error in the sky flux should not significantly affect our conclusions.

## 2.5. CryoCam Galaxy Spectroscopy

Spectra of the two galaxies G11 and G13 reported by Kirhakos et al. (1994) were obtained with the Mayall 4-m telescope at Kitt Peak National Observatory on 15 February 1999. The CryoCam spectrograph was used with the 730 Grism, which yielded an approximate wavelength coverage of 5500–10,000 Å. The slit was oriented at a position angle of  $145^\circ$  in order to simultaneously place both galaxies in the slit.

The raw data were processed using the IRAF CCDPROC package. Four exposures of 2700 seconds each were obtained. The four two-dimensional images of the spectra were compared, and using the positions of the night sky lines it was verified that the line centers were stable at the sub-pixel level. Thus, we combined the four exposures in the image plane using the IRAF IMCOMBINE task rather than extracting and combining the one-dimensional spectra. The spectra were then extracted using the IRAF task APALL.

### 3. Data Analysis

#### 3.1. Absorption Line Systems

##### 3.1.1. Optical Wavelengths

The three absorption systems, designated A, B, and C, were originally identified based upon the MgII kinematics at redshifts  $z = 0.9254$ ,  $z = 0.9276$ , and  $z = 0.9342$  in the HIRES spectrum (Churchill & Charlton 1999). In the top three panels of Figure 1, we present the absorption profiles in the rest-frame velocity of system B. The velocity zero point is defined at  $z = 0.927602$ . Twelve Voigt profile (VP) components were used to model the MgII profiles (Churchill & Charlton 1999; Churchill & Vogt 2001). The solid curve through the data are the model spectra based upon AUTOVP MINFIT, where the numbered ticks above the continuum provide the component numbers. We will refer to these numbers throughout our discussion in order to facilitate the identity of individual “MgII clouds”.

In Table 1, we list, for each of the three systems, the rest-frame equivalent widths (and  $3\sigma$  limits for non-detections) of the MgII  $\lambda\lambda 2796, 2803$ , MgI 2853, and FeII  $\lambda 2600$  transitions. The MgII and FeII column densities obtained from the VP decomposition were presented in Churchill & Charlton (1999). The density of absorption lines associated with the three systems in the optical spectrum is relatively low, and at the resolution of HIRES, there are no blends between the systems nor interloping features from metal-line systems at other redshifts (see Jannuzi et al. 1998).

##### 3.1.2. Near Ultraviolet Wavelengths

The STIS spectrum covers Ly $\alpha$ , SiII, CII, SiIII, SiIV, CIV, and NV transitions from the three systems. These data are presented in Figures 1 and 2. The density of absorption lines in the near UV is relatively high, resulting in several blends between the three systems and also interlopers from metal-line systems at other redshifts (see Jannuzi et al. 1998). Interloper absorption is indicated with an “\*”.

In Table 1, we present the rest-frame equivalent widths and  $3\sigma$  limits for the ultraviolet absorption lines shown in Figures 1 and 2. Here, we discuss the blends and interloper identifications in the order that the transitions are presented in Figures 1 and 2.

The Ly $\alpha$  in system B is blended with Galactic FeII  $\lambda 2344$  at  $v \simeq +100$  km s $^{-1}$ . SiII  $\lambda 1260$  in system B is blended at  $v \simeq +200$  km s $^{-1}$  with SiII  $\lambda 1304$  at  $z = 0.8640$ . CII  $\lambda 1334$  in system A is blended at  $v \simeq -350$  km s $^{-1}$  with a  $z = 0.6568$  CIV  $\lambda 1551$

line, since the C IV  $\lambda 1548$  absorption at the corresponding wavelength is also found. The C II  $\lambda 1334$  in system B is affected by an unidentified blend at  $v \simeq +140 \text{ km s}^{-1}$  and in system C by an unidentified blend at  $v \simeq +950 \text{ km s}^{-1}$ . These interloping lines could be due to Ly $\alpha$ , since the Ly $\beta$  absorption at the corresponding wavelengths is detected. Absorption at  $v \sim -300 \text{ km s}^{-1}$  in Si IV  $\lambda 1394$  in system A is at least partially due to C IV  $\lambda 1548$  at  $z = 0.7338$ . The corresponding C IV  $\lambda 1551$  absorption is present at  $v \sim +230 \text{ km s}^{-1}$  in the Si IV  $\lambda 1394$  absorption of system B. The self-blending of the C IV  $\lambda\lambda 1548, 1551$  is severe; C IV  $\lambda 1548$  from system B is strongly blended with C IV  $\lambda 1551$  from system A. At  $v \simeq -600 \text{ km s}^{-1}$ , N V  $\lambda 1239$  from system A is contaminated with Galactic Fe II  $\lambda 2383$ . Also, N V  $\lambda 1243$  in system B is blended with N V  $\lambda 1239$  from system C.

### 3.1.3. Far Ultraviolet Wavelengths

We show two regions of the FOS spectrum in Figure 3. The upper panel shows the partial Lyman-limit break and high-order H I lines. Also covered are the N II  $\lambda 916$  transition and the S VI  $\lambda\lambda 933, 944$  doublet. The “three-armed” ticks identifying these transitions give the locations of systems A, B, and C, respectively from blue to red. The solid curve through the data is synthesized based upon our models (discussed below). Based on the partial Lyman-limit break, Churchill & Charlton (1999) determined that the effective optical depth,  $\tau(\text{H I}) \simeq 1$ , which arises predominately from clouds eight and nine in system B.

The lower panel in Figure 3 shows the O VI  $\lambda\lambda 1032, 1038$ , Ly $\beta$ , and C II  $\lambda 1036$  transitions. Various blends are apparent. O VI  $\lambda 1032$  in system C is blended with C II  $\lambda 1036$  in system A, as well as with some unidentified absorption, possibly a Ly $\alpha$  forest line. The O VI  $\lambda 1038$  line in system A is blended with C II  $\lambda 1036$  in system B, and O VI  $\lambda 1038$  in system B is blended with some unidentified absorption, possibly another Ly $\alpha$  forest line (see Churchill & Charlton 1999, for further details).

## 4. Galaxies in the QSO Field

### 4.1. WIYN Image

In Figure 4, we present a  $15'' \times 15''$  segment of the WIYN  $i$ -band image centered on the QSO. Four galaxies, labeled G1–G4, were detected at 9.7, 8.6, 9.7, and 14.5'', respectively. Morphologically, G1 appears to resemble a warped spiral galaxy and G2 is consistent with being an early-type galaxy. G3 and G4 are somewhat amorphous. Since we lack standard flux calibrations to perform absolute photometry directly from our images, we obtained



relative magnitudes for the four candidate absorbing galaxies. Relative to G1, we find that G2 is 0.3 magnitudes fainter, G3 is 1.9 magnitudes fainter, and G4 is 2.8 magnitudes fainter (with a  $\sim 0.1$  magnitude uncertainty).

Assuming, for the moment, that G1–G4 are at  $z \simeq 0.93$ , the corresponding impact parameters are 43, 38, 43, and  $65h^{-1}$  kpc ( $q_0 = 0.5$ ). For reference, the impact parameters of galaxies identified as MgII absorbers with  $W_r(2796) \geq 0.3 \text{ \AA}$  are observed to be distributed within  $\sim 40$  kpc of the QSO line of sight (Bergeron & Boissé 1991; Steidel 1995). Again, assuming  $z \simeq 0.93$ , we obtain rough absolute magnitudes by scaling the results of Kirhakos et al. (1994), who report a Gunn- $g$  magnitude of 21.5 for G1. Ignoring color terms, we roughly estimate luminosities of  $2L_K^*$ ,  $L_K^*$ ,  $0.2L_K^*$ , and  $0.1L_K^*$  for G1–G4, respectively. In Table 2, we have listed these inferred properties based upon the assumption of  $z \simeq 0.93$  for the four galaxies.

Based upon the results of Steidel, Dickinson, & Persson (1994) and Steidel (1995), it is statistically favorable that one or more of these galaxies hosts MgII absorption. Using the criteria for associating a galaxy with MgII absorption listed by Steidel (1995), the two most luminous galaxies (G1 and G2) effectively lie at the luminosity dependent boundary,  $38h^{-1}(L_K/L_K^*)^{0.15}$  kpc, within which we expect MgII absorption having  $W_r(2796) \geq 0.3 \text{ \AA}$ . It has not yet been directly determined whether weaker MgII absorption is found beyond this boundary for normal, bright galaxies, or if there is a sharp cut-off (however, see Bowen, Blades, & Pettini (1995) and Charlton & Churchill (1996)). Under the assumption that all weak MgII absorbers are also associated with normal, bright galaxies, Churchill et al. (1999) show that absorption with  $0.02 \leq W_r(2796) < 0.3 \text{ \AA}$  would arise at impact parameters between  $\sim 40$  and  $70h^{-1}$  kpc.

The PG 1206 + 459 sightline has several intervening metal-line absorption systems in addition to the  $z = 0.93$  complex. Indeed, we identify seven additional galaxies within a radius of  $40''$  of the QSO. Their apparent magnitudes range from 0.8 to 2.2 fainter than G1. Though there is a weak redshift dependence for determining their physical impact parameter, we estimate that they all lie in the approximate range 80–200 kpc of the sightline. This places them all outside the range where strong MgII absorption is predicted. According to Chen, Lanzetta, & Webb (2001), these are good candidates for CIV absorbers, provided they are intervening the QSO.

## 4.2. Redshifts of the Candidate Galaxies

In the CryoCam spectra, the continuum of G1 was only marginally detected and no useful spectral features were present to facilitate measurement of a redshift of the galaxy. For G2, a strong emission line was measured at  $7190 \pm 2 \text{ \AA}$  (fixed to vacuum wavelengths with a heliocentric correction for comparison to the absorption redshifts). If this line is [OII]  $\lambda 3727$ , the galaxy is at a redshift of  $0.9289 \pm 0.0005$ .

This redshift places G2 at a velocity of  $+200 \pm 80 \text{ km s}^{-1}$  relative to the velocity zero point of system B. This galaxy–absorption velocity difference is consistent with that seen in a small sample of MgII galaxies (Steidel et al. 2002). Though there is no definitive data to identify G2 as the host galaxy for system B, we favor this interpretation. If system A, or system A+B were hosted by G2, the galaxy–absorber velocity difference would extend to  $750 \text{ km s}^{-1}$ , which we find to be a less likely scenario *if there is a one-to-one absorber–galaxy correspondence*.

Additional information on the galaxy redshifts has been reported by Thimm (1995), who published a Fabry–Perot image tuned to redshifted [OII]  $\lambda 3727$  at  $z = 0.93$ . G2 is clearly present in the Thimm image. Though not discussed by Thimm (1995), a visual inspection of the image also reveals a marginal [OII] emission signal from G3<sup>8</sup>.

In conclusion, we find that G2 is at the redshift of the absorbers. Considering the absorption properties of system B and the luminous properties and impact parameter of G2, we find that a system B association is highly consistent with the population of MgII absorbers. Based upon the Thimm data, we find (albeit less definitively) that G3 is also located at the redshift of the absorbers. However, we are unable to argue a clear one-to-one association with one of the three absorption systems. We have no redshift information for the bright galaxy G1, nor for the more amorphous G4. However, the luminosity and impact parameter of G1 are consistent with it hosting strong MgII absorption. In fact, we note (see Charlton & Churchill 1996) that had G1 been the only galaxy in the field within  $\sim 10''$  of the QSO, it would have been incorporated into the “absorbing galaxy” sample of Steidel, Dickinson, & Persson (1994) and Steidel (1995) *even without a confirmed redshift*<sup>9</sup>.

---

<sup>8</sup>G. Thimm could not be contacted so that we could objectively study this image.

<sup>9</sup>Only 70% of the Steidel, Dickinson, & Persson (1994) galaxies were spectroscopically confirmed.

## 5. Methods for Modeling

We follow the general technique of Churchill & Charlton (1999). Our goal is to place constraints on the chemical and ionization conditions of the absorbing gas. Our first assumption is that the gas is in ionization equilibrium, either photoionization or collisional ionization. Our second assumption is that the gas is in a minimal number of ionization phases, where a phase is a set of clouds with metallicities and ionization parameters/densities (more on this below).

### 5.1. General Procedure

In very general terms, we proceed by first assuming the gas giving rise to MgII absorption is in photoionization equilibrium. System by system, we constrain the ionization conditions and metallicities of components (or “clouds”) 1–12, using their velocities as a kinematic template upon which to compare all the observed transitions in the HIRES, STIS, and FOS spectra. As found in Churchill & Charlton (1999), we know that the MgII clouds have fairly low ionization conditions. That is,  $n_H \simeq 0.01 \text{ cm}^{-3}$ , with the ionization fractions of Mg, Fe, C, and Si being dominated by singly ionized species.

These clouds do not give rise to the bulk of the CIV NV, and OVI absorption (see Churchill & Charlton 1999). Thus, we then model the residual absorption from these species (i.e. the observed absorption remaining in the spectra after accounting for the absorption predicted by the low-ionization cloud models) as a separate zone of high-ionization, lower density gas. We explored single phase and multiphase photoionization models, single phase and multiphase collisional ionization models, and multiphase photo + collisional ionization models to describe high-ionization gas.

Because of the excellent resolution of the kinematics, we discovered that we needed to introduce a third, intermediate-ionization phase over two narrow velocity intervals to account for some of the CIV and SiIV absorption. The absorption in these velocity intervals could not be satisfactorily described within the allowed parameter spaces of models limited to low- and high- ionization phases.

### 5.2. Photoionization Modeling

We used the photoionization code Cloudy, version 90.4 (Ferland et al. 1998). Each model cloud has constant density and plane-parallel geometry. An important parameter

describing each cloud model is the ionization parameter,  $U$ , which is defined as the ratio of the incident ionizing photon density,  $n_\gamma$ , to the number density of hydrogen,  $n_H$ . For the photoionizing flux, we used the extragalactic ultraviolet spectrum of Haardt & Madau (1996). Normalized at  $z = 1$ , the number density of ionizing photons (capable of ionizing hydrogen) incident on the model clouds is  $\log n_\gamma = -5.2$  [ $\text{cm}^{-3}$ ]. For the  $z = 1$  normalization of the Haardt & Madau (1996) spectrum, the number density of hydrogen is

$$\log n_H = -5.2 - \log U \text{ cm}^{-3}.$$

The effects of alternative spectral shapes will be discussed in § 6.4. The abundance pattern was assumed to be solar (using the standard Cloudy abundances). Alternatives to a solar pattern were explored as suggested by the data.

Input parameters to Cloudy included: i) the observed or estimated column density of a well constrained transition, ii) the metallicity,  $Z$  (expressed in units of the solar value), iii) the ionization parameter,  $U$ , and iv) the abundance pattern. For each model cloud, we record the column density of transitions typically found in QSO absorption line systems that were covered by our spectra (i.e. including transitions not formally detected and not presented in Figures 1 and 2). We also record the kinetic temperature,  $T$ , which we equate with the thermal component of the Doppler parameter,  $b_{therm}^2 = 2kT/m$ , where  $m$  is the ion mass.

We assume a turbulent component to the Doppler parameter in cases where the model cloud temperature implies a smaller value than what is measured in the spectra. This turbulent component, which we assume is identical for all species, was calculated using  $b_{\text{turb}}^2 = b_{\text{ion}}^2 - b_{\text{therm,ion}}^2$ , where “turb” and “therm” denote the turbulent and thermal components, respectively. We then have the ingredients to estimate the “total” Doppler parameter for any observed transitions by inverting this relation using the appropriate ion mass.

We converge on the range of metallicity and ionization conditions by an iterative process of comparing synthetic spectra generated for each transition with column densities and temperatures of the cloud models. These spectra were convolved with the appropriate instrumental spread functions (using FFTs) in order to directly compare with the observed spectra. For the HIRES and FOS spectra, we use a Gaussian with FWHM= 6.6 km s<sup>-1</sup> and 230 km s<sup>-1</sup>, respectively. For the STIS spectra, we used the tabulated instrumental spread function appropriate for the E230M grating as published on STIS performance web pages at [www.stsci.edu](http://www.stsci.edu).

For each iteration, the synthetic spectra are superimposed on the observed spectra. A pixel by pixel  $\chi^2$  was calculated as an indicator of the quality of the overall match. However, the value of  $\chi^2$  was often dominated by large values in a very small fraction of “bad” pixels

(i.e. those having correlated noise spikes or an interloping line blend). This rendered any objective  $\chi^2$  minimization scheme fairly ineffective, since it yielded a very flat “ $\chi^2$  landscape”. Visual inspection, guided by  $\chi^2$  minimization, was essential for comparing the full kinematic profile shapes in the synthetic spectra to the observational spectra.

As described in Appendix A of Churchill & Charlton (1999), the ionization parameter was generally constrained by the relative strength of the metal–line transitions and the metallicity by Ly $\alpha$ , higher order Lyman series lines, and Lyman break from the FOS spectrum. Generally, this method yields both  $\log U$  and  $\log Z$  constrained within  $\simeq 0.1$  dex (for the assumed abundance pattern and kinematic parameterization of the profiles).

### 5.3. Collisional Ionization Modeling

We used the collisional ionization equilibrium models of Sutherland et al. (1993). These models have a solar abundance pattern. The two free parameters in these models are the kinetic temperature,  $T$ , and metallicity,  $Z$ . The ion fractions for each transition are a unique function of temperature from the models.

Given the metallicity,  $Z$ , and a measured or estimated column density of a given species,  $N^i$ , the total H column density was determined using  $N(H) = N^i / (A * Z * r^i)$ , where  $A$  is the fractional abundance of the element relative to hydrogen in a solar abundance pattern and  $r^i$  is the ion fraction of the species. Then, column densities of various species could be calculated using  $N_X^i = N(H) * A_X * Z * r_X^i$ , where  $N_X^i$  is the column density of an arbitrary species.

The Doppler parameter of each ion could be obtained in the same way as for the photoionization model, with  $T$  being the collisional temperature. In the case where the observed Doppler parameter of the optimized species was consistent with  $b^2 = 2kT/m$ , then  $b_{\text{turb}} = 0 \text{ km s}^{-1}$  was used for all ions. Similar to the procedure for photoionization modeling, we generated synthetic model spectra and superimposed them upon the data for comparison.

### 5.4. Defining and Modeling Phases

A main goal of our modeling is to parameterize the gas in as few ionization “phases” as possible. In practice, the data require at least three phases.

#### 5.4.1. Low Ionization

We define the term “MgII phase” to denote the ionization conditions which predominantly (or fully) describe the density and ionization balance of the gas giving rise to MgII absorption. For our models, this phase is characterized by number densities in the relatively narrow range  $-2.7 \lesssim \log n_H \lesssim -2.0 \text{ cm}^{-3}$ , ionization parameters in the range  $-3.2 \lesssim \log U \lesssim -2.5$  and hydrogen Doppler parameters of  $15 \lesssim b(\text{H}) \lesssim 25 \text{ km s}^{-1}$ .

The metallicity and ionization parameter were explored over the range  $\log Z$  from  $-2$  to  $0.5$  in intervals of  $0.1$  dex and  $\log U$  from  $-3.5$  to  $0$  in intervals of  $0.1$  dex. To begin, we assumed that for each system, all the MgII clouds in that system have the same metallicity and abundance pattern. This assumption is likely to not reflect reality (e.g. Ganguly, Churchill, & Charlton (1998)), but in the absence of resolved higher order HI transitions, there are virtually no constraints on the cloud to cloud metallicities. However, we explored variations in the abundance pattern as suggested by the data.

We “optimized” each cloud model on the MgII column density for trial  $U$  and  $Z$ . Recall that column densities of the MgII clouds were obtained from the Voigt profile fits (Churchill & Vogt 2001; Churchill & Charlton 1999). In its optimized mode, Cloudy adjusts  $N(\text{HI})$ , until the  $N(\text{MgII})$  of the model cloud differs from the measured value by less than a specified percent difference (we chose 5%).

#### 5.4.2. High Ionization

Analogous to “MgII phase”, we use the term “diffuse phase” to denote the gas with significantly lower density and higher ionization balance. The conditions describing this phase were less constrained than those describing the MgII phase. For our photoionization models, the diffuse phase is characterized by number densities in the range  $-4.7 \lesssim \log n_H \lesssim -3.6 \text{ cm}^{-3}$ , ionization parameters in the range  $-1.6 \lesssim \log U \lesssim -0.5$  and hydrogen Doppler parameters in the range  $20 \lesssim b(\text{H}) \lesssim 50 \text{ km s}^{-1}$ .

It was difficult to obtain a velocity template for the diffuse phase. The NV doublet in system A had sufficient velocity structure (from  $-450$  to  $-150 \text{ km s}^{-1}$ ) and signal-to-noise ratio to perform a formal automated VP fit. However, for system B, we had to use a “by-hand” method PROFIT to estimate VP fit parameters. The NV and CIV profiles provided the best constraints for ionization parameters of clouds in this phase. We followed the procedures described in § 5.4.1 to obtain a synthetic spectrum for each of the other observed transitions. The ionization parameter was tuned to attempt to produce CIV, NV, and OVI in this phase, without overproducing SiIV and other intermediate-ionization transitions. The

metallicity was constrained mainly by the Ly $\alpha$  profile.

### 5.4.3. *Intermediate Ionization*

Procedurally, we approach each system by first constraining the conditions of the MgII phase, and then the diffuse phase. However, unaccounted absorption still appeared in some individual transitions at certain velocities, particularly in transitions with intermediate-ionization state. Examples are the CIV profiles at  $v \sim -157$  km s $^{-1}$  and the SiIV profiles at  $v \sim +66$  km s $^{-1}$ . Therefore, additional clouds with intermediate-ionization states were considered.

Both photoionization and collisional ionization were explored. In the case of photoionization, Cloudy was run, optimized on the measured CIV or SiIV column density. The range of ionization parameters (for photoionization) and temperatures (for collisional ionization) were found so that no other transitions would be overproduced. Metallicity was constrained by Ly $\alpha$  and the higher order Lyman series lines. Additional details of the modeling techniques were identical to the descriptions in § 5.4.1 and § 5.4.2.

## 6. **Constraining the Absorber Properties**

Specific constraints on the phase structure of systems A, B, and C are presented here. In the text, we discuss what ranges of parameters are consistent with the data, considering scenarios of photoionization and of collisional ionization for the various required phases. For each photoionized phase we discuss constraints on the ionization parameter and metallicity, and mention the transitions that allow us to place these constraints. For collisionally ionized phases, we similarly place constraints on the temperature and metallicity.

In Tables 3–5, we give more detailed information for examples of acceptable photoionized and collisionally ionized model phases. These can be considered loosely as “best models”, intermediate in the allowed ranges. For each model, we list metallicities, ionization parameters, densities, sizes, and temperatures of model clouds for systems A, B, and C, respectively. We also list the column densities, and Doppler parameters of selected species.

In Figures 5–7 we present the data with the synthetic spectra from the “best models” superimposed. The clouds are identified by number above the continuum of the MgII  $\lambda 2796$  profile. The synthetic spectra through the HIRES data (FeII and MgII) are derived from the Voigt profile fits. For the STIS spectra, the solid curves through the data are the full model, with contributions from the MgII, intermediate- and high-ionization phases. The

dotted-line synthetic spectra are the contribution to the absorption profiles from the MgII phase only. The dashed-dot line synthetic spectra are for the intermediate-ionization phase, and the dashed-line spectra are for the high-ionization phase.

## 6.1. Constraining System A Properties

### 6.1.1. MgII Phase

The ionization parameters,  $\log U$ , of the six MgII clouds of system A were constrained by optimizing on the MgII column density from the VP fit, and adjusting  $\log U$  to best fit other low- and intermediate-ionization transitions. In order to minimize the number of phases, we assume that as much SiIV as possible is produced in the MgII clouds. (The SiIV components are too narrow to be produced in the high-ionization phase.) Thus, ionization parameters of the MgII clouds are mainly constrained by the fit to SiIV  $\lambda 1403$ <sup>10</sup>. The ionization parameters for the six clouds, MgII-1 through MgII-6, are within the range,  $-2.8 \lesssim \log U \lesssim -2.5$ , as listed in Table 3.

These values of  $\log U$  produce absorption consistent with the data in other low-ionization transitions, such as SiII and SiIII, and with the limit set by the undetected FeII. (see the dotted curve in Figure 5). However, CII  $\lambda 1334$  appears to be underproduced by such models. This is partly due to contamination ( $-360 \lesssim v \lesssim -340 \text{ km s}^{-1}$ ) by a blend with CIV  $\lambda 1551$  at  $z = 0.6568$  (see § 3.1.2). However, the underproduction at  $-420 \lesssim v \lesssim -400 \text{ km s}^{-1}$  still remains unexplained, and suggests an abundance pattern that deviates from solar. In order to fit the CII spectra we would need to increase carbon abundance by 0.4–0.8 dex in the various clouds.

Using  $-2.8 \lesssim \log U \lesssim -2.5$  and a solar abundance pattern, with the assumption that the six MgII clouds have the same metallicity, a super-solar metallicity of  $\log Z \simeq 0.5$  produced the best fit to the Lyman series lines ( $\text{Ly}\beta$  and the higher order lines; see Figure 3). To achieve a comparable fit with  $\log Z = 0.0$ , we would need to increase the abundance of magnesium by 1.0 dex (the usual “trade-off” between metallicity and abundance pattern does not apply for supersolar metallicities). If the increased abundance of magnesium was due to an  $\alpha$ -group enhancement, then silicon would be increased as well, but carbon would not (Lauroesch et al. 1996). With carbon decreased relative to magnesium by  $\sim 1.0$  dex, the discrepancy between  $\log Z = 0.0$  model and the CII profiles would be considerably more extreme.

---

<sup>10</sup>As mentioned in § 3.1.2, SiIV  $\lambda 1394$  is contaminated with CIV  $\lambda 1548$  from a system at  $z = 0.7738$



We therefore favor models with  $\log Z \simeq 0.5$  and roughly solar abundance patterns. For this  $\log Z$ , the blue side of the Ly $\alpha$  profile is underproduced. A  $\log Z \simeq 0.0$  would produce an adequate fit to Ly $\alpha$ , but would severely overproduce the other Lyman series lines. A high-ionization phase capable of fitting the blue side of the Ly $\alpha$  profile will be discussed in § 6.1.2.

The column densities of HI for these MgII clouds fall within the range  $14.4 \lesssim \log N(\text{HI}) \lesssim 15.1$  [ $\text{cm}^{-2}$ ]. Thus, this low-ionization phase in system A makes an insignificant contribution to the observed partial Lyman limit break, which requires an HI column density of  $\log N(\text{HI}) \sim 17$  [ $\text{cm}^{-2}$ ]. Given the number density  $n_H$ ,

$$\log n_H = -5.2 - \log U,$$

and the total column density of hydrogen  $N_{\text{tot}}(\text{H})$ , for  $\log Z = 0.5$  the sizes of the six MgII clouds are within 5–20 pc, using  $l = N_{\text{tot}}(\text{H}) / n_H$ .

### 6.1.2. Diffuse Phase

The strong absorption in the CIV, NV, and OVI profiles (see Figure 5), which is not fully accounted for by the MgII phase, requires a diffuse phase. Also, the blue side of the Ly $\alpha$  profile could not be fit by the MgII cloud contribution without overproducing Ly $\beta$  and the higher order Lyman series lines.

We explored both the possibility of photoionization and of collisional ionization for the diffuse phase. For the photoionization models, we optimized on the seven NV column densities given by AUTOVP MINFIT. The Doppler parameters from the VP fit were in the range  $3 \lesssim b(\text{N}) \lesssim 21$  km s $^{-1}$ , as listed in Table 3 under “Case A: Photoionization”. Collisional ionization of NV would require  $b(\text{N}) \geq 15$  km s $^{-1}$ . Therefore, for collisional ionization models we adjusted  $b(\text{N})$  and  $N(\text{NV})$  of the VP fit components using PROFIT so that all of the Doppler parameters exceeded 15 km s $^{-1}$ , as listed in Table 3 under “Case B: Collisional Ionization”. This fit for a collisional ionization phase case was plausible, but not unique.

For the case of photoionization (Case A in Table 3), CIV, NV, and OVI could arise in the same phase. Optimizing on  $N(\text{NV})$ , we found that the ionization parameters of the high-ionization phase clouds are constrained to be within the range  $-1.5 \lesssim \log U \lesssim -0.6$ . Clouds NV–1 and NV–3 have higher ionization parameters ( $\log U \simeq -0.6$ ) and are the primary producers of OVI. The other five diffuse clouds, with lower ionization parameters ( $-1.5 \lesssim \log U \lesssim -1.2$ ), give rise to the CIV absorption.

To derive constraints on metallicity for the photoionized case, we assume that the seven clouds have the same metallicity and that they have a solar abundance pattern. A metallicity of  $\log Z \simeq 0.5$  is required to fit the blue side of the Ly $\alpha$  line. This Ly $\alpha$  absorption is produced dominantly by cloud NV–2 (see Table 3), so it is important to note that the metallicities of the individual diffuse phase components are not well–constrained. The inferred metallicity of  $\log Z \simeq 0.5$  could be reduced to solar if nitrogen was enhanced by  $\sim 0.5$  dex. The properties of the seven diffuse, photoionized clouds (with sizes 1–65 kpc) are listed in Table 3.

The case of collisional ionization is more complicated. The CIV, NV, and OVI cannot be produced in a single temperature collisionally ionized model. We explored the scenario (Case B in Table 3) in which CIV is produced in the same collisionally ionized clouds as NV. The CIV and NV profiles require the temperatures of the seven clouds to be within the range  $5.14 \lesssim \log T \lesssim 5.18$  [K]. Since OVI is not produced within this temperature range, an additional phase is needed to give rise to the observed OVI absorption. The physical parameters of this additional phase are not well constrained, due to the lack of any resolvable feature in the low–resolution spectrum of OVI  $\lambda\lambda 1032, 1038$ . Therefore, we assume a single cloud, centered on the OVI absorption at the redshift  $z \sim 0.92545$ , with  $\log N(\text{OVI}) \sim 15.0$  [cm $^{-2}$ ] and  $b(\text{O}) \sim 80$  km s $^{-1}$ . This additional OVI cloud could be either photoionized or collisionally ionized. For photoionization (cloud OVI–ph), an ionization parameter of  $\log U \sim -0.6$  produces the observed OVI. This ionization parameter is high enough not to give rise to any lower–ionization transitions and low enough that the cloud remains Jeans stable. For collisional ionization (cloud OVI–co), a temperature of  $\log T \sim 5.5$  [K] would not overproduce any other transitions. Assuming that the metallicity of the OVI cloud to be the same as the clouds that in which NV arises, a metallicity of  $\log Z \simeq 0.4$  is required to fit the blue side of the Ly $\alpha$  profile.

In principle, a model in which NV and OVI are produced in a higher temperature collisionally ionized phase, and the CIV in a lower temperature collisionally ionized phase is also possible. However, it is difficult to place detailed constraints on this phase because of the blended components in the saturated CIV profiles.

We conclude that NV could be produced in a collisionally ionized phase, but that in this case an extra phase would need to be introduced to explain either the CIV or the OVI absorption. Since a single diffuse photoionized phase can be made consistent with all three high–ionization transitions, we favor a photoionized model. The dashed lines in Figure 5 represent the contribution of the photoionized diffuse phase. In § 7.5 we consider the differences between the OVI profiles for photoionization and collisional ionization models.

### 6.1.3. Intermediate Phase

Neither the MgII phase or any of the diffuse phase models could fully account for the absorption to the red of the CIV profiles (at  $v \sim -160 \text{ km s}^{-1}$ ), as shown in Figure 5. An extra component, either photoionized or collisionally ionized, thus seems necessary. For the case of photoionization, the ionization parameter is constrained to be  $\log U \simeq -2.0$ . For this ionization parameter, metallicity of  $\log Z \simeq -1.0$  is required to fill in the residual in the Ly $\alpha$  profile, at  $v \sim -125 \text{ km s}^{-1}$ . Also, a smaller value of  $\log Z$  would overproduce the higher order Lyman series lines. The contributions of this photoionized component to CIV and Ly $\alpha$  are shown as dashed-dotted curves in Figure 5. The size of the cloud is  $\sim 5 \text{ kpc}$ . Alternatively, for the case of collisional ionization, the temperature is  $\log T \sim 5.0 \text{ [K]}$ , constrained by SiIV, CIV, and NV. In this case, the metallicity of is constrained to be  $\log Z \lesssim -2.0$  to fit the residual in the Ly $\alpha$  profile.

## 6.2. Constraining System B Properties

### 6.2.1. MgII Phase

The strong, blended MgII profile in system B was fit with five narrow components ( $b \sim 5\text{--}17 \text{ km s}^{-1}$ ), spread over  $\sim 200 \text{ km s}^{-1}$  in velocity space (see Figure 6). In Table 4, the column densities and Doppler parameters from the VP fits to MgII  $\lambda\lambda 2796, 2803$  are listed for these clouds, designated as MgII–7 through MgII–11. Clouds MgII–8, MgII–9, and MgII–11 have detected FeII absorption. The ratio  $N(\text{FeII})/N(\text{MgII})$  for those three clouds thus constrains their ionization parameters to be  $\log U \simeq -3.2, -3.0,$  and  $-3.2$  (Churchill & Charlton 1999). These ionization parameters for clouds MgII–8 and MgII–9 are consistent with the absorption seen in SiII, SiIII, and SiIV. However, cloud MgII–11 does not produce a sufficient amount of SiIV to match the observed profile. An additional phase is needed, as described in § 6.2.3. For the other two clouds, MgII–7 and MgII–10, the ionization conditions are determined by the strength of SiIV to be  $\log U \simeq -2.5$  and  $-2.9$ , assuming that SiIV is produced in the low-ionization phase. These values produce models consistent with the SiII and SiIII profiles, and with the FeII limit. Figure 6 shows the contribution from clouds MgII–7 through MgII–11 as a dotted line superimposed on various observed profiles.

The five MgII clouds are assumed to have the same metallicity, but the metallicity is primarily constrained by the cloud(s) that produces the strongest HI absorption. The strongest constraint on this metallicity comes from the partial Lyman limit break that is detected in the FOS spectrum. A small uncertainty ( $\pm 0.1 \text{ dex}$ ) arises because of the subjectivity in the

continuum fit to the FOS spectrum. Under the assumption of constant metallicity for the five MgII clouds,  $\log Z \simeq 0.0$  produces the best model. Clouds MgII–8 and MgII–9 have HI column densities of  $\log N(\text{HI}) \simeq 16.7$  [ $\text{cm}^{-2}$ ] and  $\log N(\text{HI}) \simeq 16.5$  [ $\text{cm}^{-2}$ ] respectively, and are the major contributors to the break. However, for  $\log Z \simeq 0.0$ , the clouds in this MgII phase do not produce sufficient absorption to account for the entire equivalent width of the Ly $\alpha$  absorption feature<sup>11</sup>. The contribution of the MgII clouds to the Ly $\alpha$  absorption can be seen as the dotted curve on the Ly $\alpha$  profile in Figure 6. For the derived metallicity and ionization parameter constraints, the five MgII clouds have sizes of 30–200 pc.

### 6.2.2. Diffuse Phase

In Figure 6, it is shown that the MgII phase makes only an insignificant contribution to CIV and NV. The OVI is covered only in the low-resolution FOS spectrum, but it is quite strong ( $W_r(\text{OVI}1032) \simeq 0.5 \text{ \AA}$ ) for this system so it also could not be produced by the MgII phase. Also, there is no structure apparent in the broad CIV and NV profiles. These facts suggest a highly ionized, diffuse phase.

A broad VP component is placed at the velocity of cloud MgII–10 so that it is centered on the smooth NV absorption feature. Although the data are noisy, the best single-cloud VP fit to NV  $\lambda\lambda 1239, 1243$  was obtained using PROFIT, with  $\log N(\text{NV}) \simeq 14.3$  [ $\text{cm}^{-2}$ ] and  $b(\text{N}) \simeq 50 \text{ km s}^{-1}$  (cloud NV–9). The CIV profile is saturated so a VP fit could not be performed, but an additional narrow component, CIV–8, with  $b(\text{C}) \sim 14 \text{ km s}^{-1}$ , was added in order to account for the absorption seen at  $v \sim -40 \text{ km s}^{-1}$  in the CIV  $\lambda 1551$  profile (Figure 2). We considered whether photoionized and/or collisionally ionized gas at these two velocities ( $v \sim -40$  and  $+31 \text{ km s}^{-1}$ ) could account for the CIV, NV, and OVI absorption.

For a photoionized model, an ionization parameter of  $\log U \simeq -1.6$  for both components produces the amount of absorption observed in the high-ionization transitions. The exception to this is NV  $\lambda 1243$ , which is blended with NV  $\lambda 1239$  from system C. The fit to NV  $\lambda 1239$  for system B, in Figure 6, is adequate. However, as shown in Figure 9, the combined model for systems B and C produces excessive absorption at  $\sim +1000 \text{ km s}^{-1}$  in the NV profile. If, by changing model parameters, the absorption is reduced to fit the system B NV  $\lambda 1243$  profile, NV  $\lambda 1239$  and CIV  $\lambda\lambda 1548, 1551$  would be underproduced. It is unclear

---

<sup>11</sup>As mentioned in § 3.1.2, Ly $\alpha$  is contaminated by Galactic FeII  $\lambda 2344$ . Based on the simultaneous VP fit performed on the other uncontaminated Galactic FeII profiles, a synthetic Galactic FeII  $\lambda 2344$  spectrum was produced and included in the model of Ly $\alpha$ .

how to resolve this discrepancy if it is still present in higher S/N data.

With the assumption that both of the broad component clouds have the same metallicity, a value of  $\log Z \simeq -0.6$  is required to fit  $\text{Ly}\alpha$ , which could not be adequately produced in the MgII clouds. The higher order Lyman series lines in the FOS spectrum are consistent with this metallicity value for the diffuse phase clouds. Therefore, the diffuse phase is constrained to have a somewhat lower metallicity than the MgII phase. The two diffuse components, NV–9 and CIV–8, do not contribute significantly to the Lyman limit break, due to their lower column densities ( $\log N(\text{HI}) \simeq 15.8 [\text{cm}^{-2}]$  and  $\log N(\text{HI}) \simeq 15.0 [\text{cm}^{-2}]$ ). The derived sizes of the two clouds are  $\sim 54$  and  $\sim 8$  kpc, respectively.

A collisionally ionized component with a single temperature could not simultaneously produce the observed CIV, NV, and OVI absorption. To minimize the overall number of clouds, we favored the model with a single photoionized, diffuse phase. However, we explored the possibility of a contribution from an additional collisional phase. If NV and OVI arise in a collisional component, CIV would have to be produced in a photoionized phase with such a low ionization parameter that it does not give rise to NV and OVI. However, this would overproduce CIII. In order not to overproduce CIII, the photoionized phase has to be so highly ionized that OVI is fully produced. Therefore, even an additional collisionally ionized phase is ruled out in this system.

### 6.2.3. Intermediate Phase

With an ionization parameter of  $\log U \simeq -3.2$ , which is constrained by the detected FeII absorption, cloud MgII–11 does not produce the observed SiIV at  $v = 66 \text{ km s}^{-1}$ . Also, the diffuse component that gives rise to the majority of CIV, NV, and OVI is much broader than the SiIV profile. An additional component, with  $b(\text{Si}) \sim 10 \text{ km s}^{-1}$ , is superimposed on cloud 11 to account for the observed SiIV profile. This component could either be photoionized (cloud SiIV–ph) or collisionally ionized (cloud SiIV–co). For the case of photoionization, the ionization parameter is determined to be  $\log U \simeq -2.5$ , constrained by CIV and SiIII. This component would have a size of  $\sim 2$  kpc. For the case of collisional ionization, the temperature is determined to be  $\log T \sim 4.8 [\text{K}]$  (near peak production for SiIV), in order not to overproduce any other transitions.

### 6.3. Constraining System C Properties

#### 6.3.1. MgII Phase

A single, unresolved MgII cloud (cloud MgII–12) with  $b(\text{Mg}) \sim 7.5 \text{ km s}^{-1}$  is separated by  $\sim 1000 \text{ km s}^{-1}$  from system B, as seen in Figure 7. SiIV and the strongest component of absorption in CIV are aligned in velocity space with MgII. However, the Ly $\alpha$  profile is not centered on the MgII cloud, and the CIV profile shows evidence for an additional “offset” cloud at  $v = +1005 \text{ km s}^{-1}$  (cloud CIV–off). There is strong OVI absorption from system C detected in the FOS spectrum (see Figure 3), however NV  $\lambda 1243$  is only detected at the  $2.7\sigma$  level in the STIS spectrum. (The NV  $\lambda 1239$  is blended with NV  $\lambda 1243$  from system B as discussed in § 3.1.2 and § 6.2.2.)

We favor a two–phase model to produce the absorption centered on the MgII cloud, one which produces absorption in transitions from MgII to CIV, and another which gives rise to the OVI absorption (discussed in § 6.3.2). However, we first consider the possibility that one phase of gas can give rise to absorption in all these transitions. With an ionization parameter  $-1.8 \lesssim \log U \lesssim -1.5$ , both SiIV and CIV can be produced in the same phase as MgII, as can the SiIII  $\lambda 1207$ . The OVI  $\lambda 1038$  (OVI  $\lambda 1032$  is blended; see § 3.1.3) can also be produced in this MgII cloud. However, a much lower ionization parameter ( $\log U \sim -3.0$ ) is required to give rise to the observed SiII  $\lambda 1260$  absorption. Furthermore, NV  $\lambda 1243$  would be severely overproduced by this model. To achieve consistency, the abundance of nitrogen would need to be decreased by  $\sim 2$  dex relative to other elements. Although nitrogen is deficient by  $\sim 1$  dex in dwarf galaxies (Mateo 1998), the required 2 dex adjustment is clearly extreme. The one–phase model would have a super–solar metallicity of  $0.2 \lesssim \log Z \lesssim 0.4$  in order to fit the red wing of Ly $\alpha$ . The size of this single MgII cloud would be 10–160 kpc. However, we conclude that the problems with SiII underproduction and NV overproduction are too severe, and that a one–phase model is excluded.

In the two–phase scenario, the MgII phase has a lower ionization parameter so that NV is not severely overproduced, but a separate high–ionization phase is needed to account for the OVI absorption. The ionization parameter of the MgII phase is constrained to be  $\log U \simeq -2.0$ . For a lower  $U$ , CIV would be underproduced. However, at this ionization parameter, SiIV is not sufficiently produced. This, together with the underproduction of SiII  $\lambda 1260$ , suggests the need for an enhancement of silicon. A 0.4 dex silicon enhancement brings the  $\log U \simeq -2.0$  model into agreement with the SiII  $\lambda 1260$  and SiIV  $\lambda\lambda 1394, 1403$  profiles. In this case, the less severe overproduction of NV can be resolved by a 0.4 dex decrease of nitrogen. At  $\log U \simeq -2.0$ , a metallicity of  $\log Z \simeq 0.1$  matches the red wing of the Ly $\alpha$  profile. This model is indicated by the dotted curve on Figure 7. The size of the

MgII cloud in this two-phase scenario is  $\sim 4$  kpc.

Of the two approaches that we have explored for the MgII phase, we favor the two-phase scenario. The one-phase scenario is consistent with our philosophy of minimizing the number of phases. However, a 2 dex deficit of nitrogen is unlikely and it seems contrived to assume that the SiII  $\lambda 1260$  profile is contaminated by a blend. The two-phase scenario requires only a modest abundance pattern adjustment (a 0.4 dex deficit for nitrogen and a 0.4 dex enhancement for silicon). This adjustment is reflected in the model results summarized in Table 5.

### 6.3.2. Diffuse Phase

A high-ionization phase is required in the two-phase scenario in order to fit the OVI. However, the physical parameters of this phase are poorly constrained due to the unresolved OVI profiles, covered in the low-resolution FOS spectrum. Both photoionization and collisional ionization could contribute to this phase.

For the case of photoionization, a grid with  $10 \lesssim b(\text{O}) \lesssim 80 \text{ km s}^{-1}$  was constructed, with various  $\log Z$  and  $\log U$  values. The ionization parameter is roughly constrained to be  $-1.0 \lesssim \log U \lesssim -0.5$ . If the ionization parameter is lower than this, NV will be overproduced; if it is any higher, the cloud will not be Jeans stable. For  $b(\text{O}) = 80 \text{ km s}^{-1}$ , NV would be overproduced unless the ionization parameter is  $\log U \gtrsim -0.5$ . The metallicity would also have to be  $\log Z \gtrsim -0.5$ , in order not to overproduce Ly $\alpha$ . As  $b$  decreases, both the metallicity and the ionization parameter can be lower. For example, for  $b(\text{O}) = 10 \text{ km s}^{-1}$ , the metallicity could reach  $\log Z \simeq -1.5$  if  $\log U \gtrsim -1$ .

For the case of collisional ionization, a similar grid was constructed, with  $10 \lesssim b(\text{O}) \lesssim 80 \text{ km s}^{-1}$  and with various  $\log Z$  and  $\log T$  values. Compared to photoionization, the profiles are less sensitive to change in  $b$  parameter and metallicity. However, the temperature is well constrained. A stringent lower limit of  $\log T \gtrsim 5.4$  [K] prevents the overproduction of NV and Ly $\alpha$ , and a rough upper limit of  $\log T \lesssim 6$  [K] prevents the overproduction of Ly $\alpha$ . For each temperature, the assumption of pure thermal broadening provides as a lower limit on the  $b$  parameter. For example, at  $\log T = 5.4$  [K],  $b(\text{O}) \gtrsim 16 \text{ km s}^{-1}$  and at  $\log T = 6$  [K],  $b(\text{O}) \gtrsim 32 \text{ km s}^{-1}$ .

Regardless of the ionization mechanism of the diffuse phase, SiIV is not significantly produced. Therefore, the assumption that SiIV arises in the MgII clouds is valid for any two-phase solution. A three-phase scenario, with the lowest-ionization phase giving rise to the majority of MgII, the intermediate-ionization phase to the majority of SiIV, and the

highest-ionization phase to OVI, is excluded. The intermediate phase would either have a high enough ionization parameter so that NV would be severely overproduced, or it would have a low enough ionization parameter so that it gives rise to the majority of the MgII. In the latter case, the original MgII phase is redundant.

### 6.3.3. Offset Phase

The Ly $\alpha$  profile is centered at a different velocity than the MgII ( $\sim 37 \text{ km s}^{-1}$  to the blue). Also, in order to produce the “wing” at the blue edge of the CIV profiles, a VP fit required an offset cloud with  $b(\text{C}) \sim 15.5 \text{ km s}^{-1}$  at  $v = +1005 \text{ km s}^{-1}$  (cloud CIV-off). Collisional ionization, for a temperature that produces CIV, yields a  $b(\text{H})$  too broad to fit the Ly $\alpha$  profile and is, thus, ruled out. For photoionization, the ionization parameter is constrained by NV to be  $-2.0 \lesssim \log U \lesssim -1.6$ . For  $\log U \simeq -2.0$ , the metallicity is constrained by the blue wing of the Ly $\alpha$  profile to be  $\log Z \simeq -1.0$ . For  $\log U \simeq -1.6$ , the metallicity is  $\log Z \simeq -1.2$ . The cloud has a size of  $\sim 5 \text{ kpc}$ . Various physical parameters of the multiple phases in this system are listed in Table 5.

## 6.4. Effects of Assumed Input Spectrum

For the photoionization models, the different spectral energy distributions (shape) of the ionizing spectrum can produce different ionization balances in the gas. Here, we report on our experimentation with other plausible shapes of the ionizing spectrum.

However, we note that for any one of the systems to be affected by stellar radiation from one of the galaxies at a galactocentric distance of  $> 38h^{-1} \text{ kpc}$  would require extreme conditions. For the most active bursting galaxy it is reasonable to assume a luminosity of ionizing photons,  $L \sim 10^{54} \text{ photons s}^{-1}$ , of which  $\sim 1\%$  escape (Hurwitz, Jelinsky, & Dixon 1997). At a distance of  $38h^{-1} \text{ kpc}$ , this corresponds to  $5 \times 10^4 \text{ photons cm}^{-2} \text{ s}^{-1}$ . This is a factor of four less than the assumed Haardt & Madau background ionizing photon flux at  $z \sim 1$  ( $2 \times 10^5 \text{ photons cm}^{-2} \text{ s}^{-1}$ ).

The [OII]  $\lambda 3727$  emission flux measured by Thimm (1995) for galaxy G2 can be used to estimate the number of ionizing photons escaping that galaxy. Any other galaxy, not detected in Thimm’s image would make a smaller contribution. Following the method of Bergeron et al. (1994), in Churchill & Charlton (1999) we estimated that the luminosity of ionizing photons in G2 is  $L \sim 3 \times 10^{53} \text{ photons s}^{-1}$ . Although, the escape fraction is highly uncertain, we note that this luminosity is a factor of three less than that of the extreme



starburst mentioned above. If an escape fraction of 1% is again assumed, this means the Thimm limit yields an ionizing photon flux a factor of twelve less than the Haardt & Madau background at 1 Rydberg.

We therefore find it unlikely that systems are *significantly* affected by local stellar radiation. Nonetheless, we briefly consider the general effects that changes in the shape of our assumed ionizing spectrum would have on the results above. Our results here agree with those in Appendix B of our previous paper on the PG 1206 + 459 absorbers (Churchill & Charlton 1999)

Starburst models with population ages of 0.01 and 0.1 Gyrs provide examples of the most extreme changes in spectral shape we might expect. We utilize the burst models of Bruzual & Charlot (1993), superimposed on the  $z = 1$  Haardt and Madau spectrum, and reconsider the results of our photoionization models. Even though they appear to be excluded based on the Thimm (1995) limits, we considered models with the stellar flux equal to the Haardt and Madau flux at 1 Rydberg.

In a 0.01 Gyr starburst model there are extreme edges due to H I, He I, and He II, leading to a soft spectrum as compared to Haardt and Madau. It is clearly impossible to produce significant amounts of C IV, N V, and O VI absorption by photoionization with this spectral shape. Therefore, the extragalactic background photons must be responsible for the high-ionization phases of the systems, unless it is collisional ionization. The low-ionization phase constraints would be slightly altered by the 0.01 Gyr starburst spectral shape. Specifically, the metallicity constraint is typically lowered by 0.5 dex. Furthermore, the Si IV could no longer be produced primarily in this phase and additional intermediate-ionization phases would be required. If subject to the same starburst spectral shape, it would be difficult to tune these intermediate-ionization phases so they would not give rise to excess low-ionization absorption.

The 0.1 Gyr burst model has an extreme H I edge, but above 1 Rydberg its shape is similar to that of the Haardt and Madau spectrum. Therefore, spectral shape differences produce small changes in the constraints on photoionized clouds as compared to the pure Haardt and Madau model. Slightly more Si IV and C IV would be produced in the low-ionization phase, which would lead to slightly lower ionization parameter constraints. The model metallicity would actually be increased because the spectral shape of the burst model provides relatively more photons at energies just above the ionization edge of H I (where the cross section is largest).

We argued that it is unlikely that anything but small stellar contributions to the ionizing flux are allowed. Having explored the effect of the resulting changes to spectral shape, we

conclude that, even if there are stellar contributions to the ionizing spectrum, this will not change our basic conclusions.

## 7. Summary and Discussion

Along the line of sight toward the quasar PG 1206 + 459 at  $z \sim 0.928$  there is a “group” of three MgII absorption systems within a velocity range of  $1500 \text{ km s}^{-1}$ . With the E230M grating of STIS on *HST*, we obtained  $R = 30,000$  spectra covering Ly $\alpha$  and various metal line transitions, most notably the high-ionization transitions of SiIV, CIV, and NV. These complement our previous  $R = 45,000$  Keck/HIRES spectra that showed low-ionization clouds in MgII and FeII. We assume that these clouds are slabs, photoionized by the extragalactic background (Haardt & Madau 1996), and constrain their physical conditions. We consider any role that collisional ionization may play in the observed absorption properties. To account for the entire ensemble of chemical transitions in each system requires several phases of gas, each with different densities. We also analyzed a WIYN image of the quasar field and found four galaxies within  $15''$  of the line of sight. The redshift of one of the galaxies was obtained from long-slit spectra from the KPNO 4-m telescope.

In § 7.1–7.3, we will first summarize the physical conditions that we have found for each system. We will also compare to our previous results based on the low-resolution FOS spectra (Churchill & Charlton 1999), and to other absorption systems studied at high resolution. In § 7.4, we will analyze the high-ionization phases of these systems using methods similar to those applied in the study of Milky Way high-ionization gas. The goal of that analysis is to make comparisons with the Milky Way corona and to assess whether simple photoionization models can realistically give rise to the high-ionization absorption. Finally, in § 7.5, in the context of our photoionization and collisional ionization models, we present predictions for the appearance of the OVI profiles that could be observed at high resolution with Cosmic Origin Spectrograph (COS), to be commissioned in the 4th servicing mission of *HST*.

### 7.1. System A

System A, if it were separated from system B, would be classified as a multiple-cloud, weak MgII absorber with  $W_r(2796) \sim 0.22 \pm 0.02 \text{ \AA}$  (Churchill et al. 1999; Churchill & Vogt 2001). The six MgII components in system A are consistent with being produced by 5–20 pc clouds with  $-2.8 \lesssim \log U \lesssim -2.5$ . The metallicity of these clouds would be  $\log Z \simeq 0.5$ , with the assumption of a solar abundance pattern. The NV profiles are strong and highly

structured. Both photoionization and collisional ionization models can consistently fit the profiles, but collisional ionization models require two finely tuned high-ionization phases. We therefore favor photoionization for the diffuse phase. Photoionized regions with sizes of 1–65 kpc, and with  $-1.5 \lesssim \log U \lesssim -0.6$ , could produce the NV as well as the strong CIV and OVI absorption. This system does not contribute significantly to the Lyman limit break, again distinguishing it from strong MgII absorbers (Churchill et al. 2000a).

Based on the low-resolution FOS spectrum, Churchill & Charlton (1999) were unable to determine whether the high-ionization gas is consistent with photoionization or collisional ionization. We have now concluded that either photoionization or collisional ionization can be consistent with the relatively narrow NV components. However, a single diffuse photoionization model producing all three high-ionization transitions CIV, NV, and OVI is favored. Our conclusions about the low-ionization phase are similar to those of our previous study, except that we infer a slightly lower ionization parameter ( $-2.8 \lesssim \log U \lesssim -2.5$  as compared to  $\log U \sim -2.5$ ). This is because we have determined that the SiIV  $\lambda 1394$  profile, which is relatively strong in the FOS spectrum, is contaminated by CIV  $\lambda 1548$  at  $z = 0.7338$ . Therefore, we now use the unblended, weaker SiIV  $\lambda 1403$  transition in the STIS spectrum as our constraint.

System A could be associated with one of the galaxies detected in our WIYN image of the quasar field (Figure 4). G2 is believed to be associated with system B (see § 7.2) and G4 is at a much larger impact parameter than the other three galaxies. Therefore, G1 and G3, both at an impact parameter of  $43h^{-1}$  kpc, are the most likely host galaxy candidates. They are just beyond the boundary of  $38h^{-1}(L_K/L_K^*)^{0.15}$  kpc, within which strong MgII absorption is commonly detected (Bergeron & Boissé 1991; Bergeron et al. 1992; Le Brun et al. 1993; Steidel, Dickinson, & Persson 1994; Steidel 1995; Steidel et al. 1997). G1 appears to be a  $\sim 2L^*$  spiral galaxy with a warped disk structure and G3 is less luminous ( $\sim 0.2L^*$ ), without apparent morphology.

Both in terms of its MgII equivalent width and the impact parameter of its candidate host galaxies, system A is just below the threshold for strong MgII absorption. It is reasonable to infer that such a system could arise either in a dwarf galaxy or in the outskirts of a giant galaxy. Because the metallicity is supersolar in this case, the former possibility seems less likely (Mateo 1998). We favor that system A is more likely to arise from a patchy distribution of gas in the outskirts of the apparently warped, spiral disk, G1 in Figure 4. The high metallicity and large diffuse phase absorption suggest a local environment with active star formation. Tidal debris, relating to interactions between the galaxies in a group, is one possibility.

Multiple-cloud, weak MgII absorbers may be a varied population in terms of their

origins. A counter-example to system A is the multiple-cloud, weak MgII absorber at  $z = 1.0414$  along the line of sight toward PG 1634+706 (Zonak et al. 2003). In that case, a low metallicity of  $\log Z \sim -1.5$  and the relative kinematics of the low- and high-ionization gas suggest an origin in a pair of dwarf galaxies, a dwarf superwind, or a lower metallicity outer disk region. That system also differs from system A in that it produces a partial Lyman limit break.

The most unusual thing about system A is its very strong high-ionization absorption and, in particular, the structure in NV. If the host galaxy is, in fact, the spiral galaxy, G1, we might expect some similarities with the high-ionization gas phases around the Milky Way. We examined the  $\sim 20$  archival *HST* E140M spectra of AGNs and quasars that are suitable for study of the Galactic NV absorption. Only five had detected Galactic NV (H 1821 + 643, NGC 3783, 3C 273, Mrk 509, and NGC 5548), and of these only H 1821 + 643 showed relatively narrow components similar to those in system A. The H 1821 + 643 line of sight has been studied in detail (Bahcall et al. 1993; Savage et al. 1995; Oegerle et al. 2000; Tripp et al. 2001). The NV absorption, at  $v = -8 \text{ km s}^{-1}$ , arises within several kpc of the Sun, quite possibly from the outer boundary of radio loop III (Savage et al. 1995). The relatively small ratio,  $N(\text{CIV})/N(\text{NV})$ , is consistent with conditions expected for collisionally ionized gas in a cooling supernova bubble (Slavin & Cox 1992, 1993). The NV components in system A are even narrower than this special case, although they are still consistent with an origin in collisionally ionized gas. As discussed in § 6.1.2, however, if the NV is produced by collisional ionization, either the CIV or the OVI would have to arise in a separate phase.

We conclude that the high-ionization phase of system A differs from those along lines of sight from our vantage point in the Milky Way. The complex kinematics of the high-ionization gas in system A is suggestive of dynamic processes perhaps related to interactions (e.g. Bowen, Blades, & Pettini (1995)). To understand the physical environment of system A, we must search for common elements between its galaxy host properties and those of the hosts of other similar absorption systems yet to be discovered.

## 7.2. System B

System B, if isolated from system A, would be a classic, strong MgII absorber with  $W_r(2796) \sim 0.66 \pm 0.01 \text{ \AA}$  (Churchill & Vogt 2001). It gives rise to a partial Lyman limit break. Five blended MgII clouds, with  $-3.2 \lesssim \log U \lesssim -2.5$  and sizes of 30–200 pc, are constrained by the Lyman limit break to have  $\log Z \simeq 0.0$ . The cloud farthest to the red ( $\sim +50 \text{ km s}^{-1}$ ) has strong, broader SiIV, which requires an additional, intermediate-ionization phase (photoionized with  $\log U \simeq -2.5$  or collisionally ionized with  $\log T \sim 4.8 \text{ [K]}$ ). The

NV absorption profiles are broad ( $b(\text{N}) \sim 50 \text{ km s}^{-1}$ ), and relatively smooth. They are consistent with being produced in a  $\sim 50 \text{ kpc}$  cloud, with  $\log U \simeq -1.6$  and  $\log Z \simeq -0.6$ . The saturated CIV profiles require an additional  $b(\text{C}) \sim 13 \text{ km s}^{-1}$  component, offset to the blue.

Our results for system B agree with our previous conclusions based on the low-resolution FOS spectra (Churchill & Charlton 1999). The properties of both the low- and high-ionization phases are very similar. With the higher-resolution SiIV profiles, we are now able to diagnose its origin in an additional phase. Previously, we were able to account for the overall strength of SiIV by tuning the ionization parameter of the MgII clouds.

An  $\sim L^*$  galaxy at  $z \simeq 0.929$ , at an impact parameter of  $38h^{-1} \text{ kpc}$  (G2 in Figure 4), is believed to be associated with system B. The galaxy does not have distinguishable disk structure, so its morphology is uncertain.

The smooth, broad NV absorption profile from system B is quite similar to most of the NV profiles observed along Milky Way lines of sight. For example, the line of sight toward the inner Galaxy star, HD 167756, shows a smooth, broad NV profile, and a more structured SiIV profile (Savage, Sembach, & Cardelli 1994). Perhaps more relevant are the extragalactic lines of sight, NGC 3783, 3C 273, Mrk 509, and NGC 5548, which show similar (but weaker) NV absorption. In our Galaxy, the NV absorption is consistent with arising in an exponential distribution centered around the disk, with scale height  $3.9 \pm 1.4 \text{ kpc}$ , referred to as the “Galactic corona” (Savage et al. 1997).

Because of the similarities with the Milky Way, it is tempting to interpret the high-ionization gas from system B as a corona. Also, the detection of an emission line in the host galaxy of system B is evidence for star formation activity. However, there are several problems with this interpretation. First, there is no apparent disk structure in the host galaxy. Second, the impact parameter is large, and little is known about corona structure at such distances. Third, the NV absorption is extremely strong in this case. If broad, smooth, high-ionization components are characteristic of coronae then we will be likely to find them in many other strong MgII absorbers. Then, the question would be why these components are so strong in system B. Perhaps this could relate to its apparent location in a group of galaxies.

The intermediate-ionization component needed to explain the SiIV absorption deserves further comment. It appears that this type of situation, where a phase produces absorption only in one transition, is not uncommon. The  $z = 0.9902$  absorber toward PG 1634 + 706 requires an additional collisionally ionized component, with  $T \sim 60,000 \text{ K}$  to fit its SiIV profiles (Ding et al. 2003). Similarly, the SiIII profiles in the  $z = 1.0414$  system toward

PG 1634 + 706 are consistent with an additional collisional ionization phase, with  $T \sim 40,000$  K (Zonak et al. 2003). Cooling proceeds rapidly in this temperature range, so if these types of gas phases are common it would imply that formation of shock-heated regions is frequent in interstellar gas at  $z \sim 1$ .

### 7.3. System C

System C was classified as a single-cloud, weak MgII absorber, with  $W_r(2796) = 0.051 \pm 0.005$  Å (Churchill & Vogt 2001). Our favored model for system C includes two clouds at  $v \sim +1042$  km s<sup>-1</sup> and one at  $v \sim +1005$  km s<sup>-1</sup>. The MgII arises in a  $\log U \simeq -2.0$  cloud, which gives rise to most of the observed SiIV and CIV. The metallicity of this cloud is approximately solar. However, in order to produce both SiII  $\lambda 1260$  and SiIV  $\lambda 1394$ , a 0.4 dex enhancement of silicon is required. Additionally, a 0.4 dex reduction of nitrogen is needed to bring the model prediction into agreement with the data. In our favored model, the bulk of the OVI arises in a more highly ionized phase, whose properties are not well constrained because we lack high-resolution coverage of OVI. The cloud at  $v \sim 1005$  km s<sup>-1</sup> has an ionization parameter  $\log U \simeq -1.6$  and a metallicity of  $\log Z \sim -1.2$ . It is required to produce the blue wing of Ly $\alpha$  as well as the asymmetry in CIV.

In our previous work (Churchill & Charlton 1999), based on the low-resolution FOS spectra, we concluded that the CIV absorption could not all be produced in the same phase as the MgII. However, we could not distinguish whether the two transitions were aligned in velocity space. Now, we see that an offset CIV cloud is needed to explain the asymmetric CIV profiles. The offset cloud led to a broad CIV profile in the low-resolution data, and this was the main reason we found a one-phase model to be inconsistent with the low-resolution data. However, for more subtle reasons, in our present analysis we also favor a model with two separate phases centered on the MgII.

Since several galaxies were found at relatively small impact parameter, it is likely that system C is also related to one of these galaxies, either G1 or G3. Since we argued in § 7.1 that G1 was more likely to host system A, by process of elimination we consider G3 the more likely host for system C. With a luminosity of  $\sim 0.2L^*$  and an impact parameter of  $43h^{-1}$  kpc, statistically, this galaxy would be unlikely to produce strong MgII absorption. However, either G3 itself or a high-velocity cloud or satellite related to G3, could be responsible for this weaker MgII system. The average value of the OVI column density in the Small Magellanic Cloud is 1.7 times higher than the average value in the Milky Way (Hoopes et al. 2002). The relatively large, high-ionization absorption from system C could plausibly come from a similar satellite galaxy.

Single–cloud, weak MgII absorption appears to arise in a variety of environments. Clouds with  $W_r(2796) \sim 0.1 \text{ \AA}$  are found, both isolated in velocity space (Churchill et al. 1999) and clustered within hundreds of  $\text{km s}^{-1}$  of strong MgII absorbers (Churchill & Vogt 2001). System C is an extreme case in that it is a full  $1000 \text{ km s}^{-1}$  from system B. Single–cloud, weak MgII absorption is also detected in some Milky Way high–velocity clouds (Churchill, Charlton, & Masiero 2002). At least some of the isolated, single–cloud weak MgII absorbers appears to trace tiny star–forming pockets separate from  $L^*$  galaxies (Rigby et al. 2002). They could arise in faded dwarf galaxies or in remnants of Population III star clusters. The nature of the high–velocity clouds also remains a mystery: are they ejected from the Milky Way disk, or are they primordial clouds falling into the Local Group? (see, e.g., Wakker & van Woerden (1997), Blitz (2002), and Putman et al. (2002)). More generally, the question is whether the various weak MgII absorption profiles are produced by the same physical structures in different environments, or whether the similarity of their MgII profiles is just a coincidence.

We compare system C to the three isolated, single–cloud, weak MgII absorbers along the line of sight toward PG 1634 + 706 (Ding et al. 2003). All three of them have close to solar metallicity, similar to system C, and two of them require additional high–ionization clouds, offset in velocity. However, they differ from system C in that they all require a lower–ionization phase in which the MgII absorption arises (with  $-4.5 \lesssim \log U \lesssim -2.7$ ) and a separate high–ionization phase (with  $-2.5 \lesssim \log U \lesssim -1.5$ ) to produce the CIV absorption centered on the MgII. It is interesting that the phase that produces MgII absorption for system C (with  $\log U \sim -2.0$ ) is more similar to the high–ionization phase for the three isolated, single–cloud, weak MgII absorbers. The size of the MgII cloud in system C is 4 kpc, while the low–ionization clouds that produce isolated, single–cloud weak MgII absorbers are quite small (pcs or tens of pcs).

Another interesting comparison is to the individual MgII clouds in system A, since they each have about the same equivalent width as system C. There are small differences in the inferred properties of the phases giving rise to MgII. System A clouds generally have a slightly lower  $U$ , a slightly higher (supersolar) metallicity, and smaller  $b$  parameters. However, the most striking difference is between the high–ionization diffuse phases. The separate, diffuse clouds of system A have very strong NV absorption, but NV is not detected in system C. In fact, system C is the more typical absorber, since the NV absorption is unusually strong in system A (and system B).

There is presently little direct information published about the physical conditions of the gas in “satellite clouds” of strong MgII absorbers at  $z \sim 1$  which are found within hundreds of  $\text{km s}^{-1}$  of the dominant absorption component. It is likely that they are sub–Lyman

limit systems (Churchill & Vogt 2001), and many have a resolved C IV component separate from that related to the dominant, low-ionization component (based upon our unpublished STIS data). Some also have detected O VI. In principal, system C could simply be a similar satellite cloud, though at a much larger velocity separation than the others.

A related comparison is to the high-velocity clouds around the Milky Way, not those that are detected by 21-cm emission, but those that are below that threshold and are detected through absorption in various metal transitions. The Galactic HVCs are a varied population in terms of the phase structure, with some having strong low-ionization absorption and others having only high-ionization absorption (Sembach et al. 1999). Some systematic differences between Milky Way HVCs and those at  $z \sim 1$  are to be expected because the extragalactic background contribution has decreased substantially since  $z \sim 1$  (Haardt & Madau 1996). In particular, some Milky Way HVCs are detected only in low-ionization transitions, which could be explained by a stellar contribution to the ionizing spectrum. However, the “satellite clouds” around strong Mg II absorbers at  $z \sim 1$  and the HVCs around the Milky Way could really be the same population (Churchill & Vogt 2001; Churchill, Charlton, & Masiero 2002).

In conclusion, the physical conditions we inferred for system C could be consistent with it arising in the same type of structure that produces satellite absorption at smaller velocities around various strong Mg II absorbers. These conditions are not consistent with the properties of isolated, weak Mg II absorbers (Rigby et al. 2002; Charlton et al. 2002). In order that the probability of intercepting a high-velocity cloud at  $+1000 \text{ km s}^{-1}$  is not vanishingly small (e.g. among the 22 high-velocity clouds in Churchill & Vogt (2001), the 2 with the highest velocity are at  $\sim \pm 410 \text{ km s}^{-1}$ ), there would have to be an abundant population of these objects in the PG 1206 + 459  $z \sim 0.93$  group, and their cross section would have to be large.

#### 7.4. Nature of the High-Ionization Phases

Because of inefficiencies of observing in the ultraviolet, there are very few examples of high-resolution quasar absorption line systems at  $z \sim 1$  with high-resolution spectra covering many transitions. By far, the most extensive body of detailed work analyzing spectra probing interstellar medium and halo gas comes from studies of our Galaxy. Savage et al. (1997) considered the mechanisms responsible for producing and maintaining the Galactic corona. In particular, they determined the apparent column density ratios of Si IV, C IV, and NV at various scale-heights from the disk, and in various directions. They argued that a simple photoionization or collisional ionization model could not reproduce the range of observed values, and compared their observations to results from models of more complex,



non-equilibrium processes. The conclusion of their work was that a hybrid model that includes some combination of several such processes (e.g., Galactic fountain gas, gas related to supernova bubbles, and turbulent mixing layers of hot and warm gas) is needed.

We can compare the properties of the high-ionization gas phases of systems A, B, and C to those of the gas around the Galaxy. To facilitate this comparison, we calculated the apparent column densities of SiIV, CIV, and NV as a function of velocity along the PG 1206 + 459 line of sight. The apparent column density of a given transition at velocity  $v$  is given (as in Savage & Sembach (1991)) by

$$N_a(v)[\text{cm}^{-2}(\text{km s}^{-1})^{-1}] = (m_e c / \pi e^2) (f \lambda)^{-1} \tau_a(v),$$

where  $f$  is the oscillator strength of the transition and  $\lambda$  is in  $\text{\AA}$ . The apparent optical depth,  $\tau_a(v)$  is given by

$$\tau_a(v) = \ln[1/I_{norm}(v)],$$

where  $I_{norm}$  is the normalized flux. Values of  $N_a(v)$  were obtained in every pixel in which a transition was detected at a  $3\sigma$  level. Otherwise, limits were derived by replacing  $I_{norm}(v)$  by  $1 - \sigma(v)$ , where  $\sigma(v)$  is the  $1\sigma$  error bar on the flux. We computed  $N_a(v)$  for SiIV  $\lambda\lambda 1394, 1403$ , CIV  $\lambda\lambda 1548, 1551$ , and NV  $\lambda\lambda 1239, 1243$ . For each doublet, a single apparent column density value was derived based on the following rules: 1) if neither transition was saturated, the  $N_a(v)$  values were averaged; 2) if only the stronger member of the doublet was saturated we used the weaker member; and 3) if both members of the doublet were saturated, we used the weaker member to set a lower limit. Measurements or limits for the ratios  $N_a(\text{CIV})/N_a(\text{SiIV})$ ,  $N_a(\text{CIV})/N_a(\text{NV})$ , and  $N_a(\text{SiIV})/N_a(\text{NV})$  were determined in regions where at least one transition was detected. These ratios, with  $1\sigma$  errors or limits where appropriate, are shown as a function of velocity, in Figure 8.

The apparent column density ratios for systems A, B, and C can be directly compared to those found in our Galaxy (Figure 6 of Savage et al. (1997)). In general, systems A and B have  $N_a(\text{CIV})/N_a(\text{SiIV})$  much larger and  $N_a(\text{SiIV})/N_a(\text{NV})$  much smaller than any Milky Way line of sight. Taken at face value, all three ratios are consistent only with the “interface/bubble” model and not with “fountains” or with “mixing layers” (for details and references on the different models, see Savage et al. (1997)). In system C, NV is not detected, but the lower limits on  $N_a(\text{SiIV})/N_a(\text{NV})$  and  $N_a(\text{CIV})/N_a(\text{NV})$ , and the large value of  $N_a(\text{CIV})/N_a(\text{SiIV})$  are consistent only with the “mixing layers” model.

We need to be cautious about this simple interpretation. Figure 8 also shows, as solid pentagons, the ratios of the cloud column densities for the high-ionization phase of our model. In our models for all three systems, SiIV is found primarily in the low-ionization component, so  $N_a(\text{CIV})/N_a(\text{SiIV})$  is off scale for the high-ionization components. For the

low-ionization component,  $N_a(\text{CIV})/N_a(\text{SiIV}) \sim 2$  for systems A and B. The observed values are actually in between those of the two model phases. This is not unexpected, since we are averaging along a line of sight that is likely to pass through many types of regions. It is interesting to note that, even for our Galaxy, the OVI column density varies by factors of several on scales of hundreds of parsecs (Howk et al. 2002). Since the high-ionization gas has such a patchy distribution, we would expect the local apparent column density ratios to vary significantly from the global value.

We conclude, that if the gas is in a complex set of phases along an extended line of sight, as we have proposed, it is inappropriate to directly compare the observed apparent column density ratios to any models. For the Milky Way, the interpretation is aided by the fact that specific regions can be isolated in velocity space, and “local” apparent column density ratios can be considered. For extragalactic absorption systems, understanding the phase structure is critical to isolating the regions, and therefore to interpreting what processes are involved in producing and maintaining the high-ionization gas.

### 7.5. Expectations for High-Resolution OVI Profiles

It is a bit surprising that simple photoionization models can consistently produce the absorption observed in all of the high-ionization transitions. This is especially true, in view of the fact that such simple models fail to explain the Milky Way corona (Savage et al. 1997). Fortunately, a test of the simple models is possible.

We have been able to place good constraints on the properties of the photoionized high-ionization phases based particularly on the SiIV, CIV, and NV transitions, as well as on the low-resolution FOS profile of OVI  $\lambda\lambda 1032, 1038$ . Though both have extremely strong absorption in high-ionization transitions, systems A and B are strikingly different. System A appears to be the unusual one because of the relatively narrow NV structures. High resolution coverage of the OVI would be essential to distinguish between collisional ionization (which is permitted by the data) and photoionization (the minimal phase model which we prefer). System B is consistent with what one would expect from corona gas, with broad, and less structured, high-ionization profiles. The model constraints for these two systems provide a very specific prediction for how the OVI  $\lambda\lambda 1032, 1038$  would look at higher resolution. Figure 9 presents the model predictions for an observation of OVI  $\lambda\lambda 1032, 1038$  using the planned COS on *HST*, which will have a resolution of  $R = 18,000$  at the observed wavelength of OVI. The solid curve represents a pure photoionization model for all three systems, as summarized in Tables 3–5. The dashed curve indicates the prediction of a collisional ionization model for system A. We find that if a simple, single-phase photoionization model

applies for system A, the OVI should have structure very similar to the NV. If a collisional ionization model applies, the OVI profiles for system A would be smooth, similar to those of system B. For the case of system C, there are a wide range of parameters allowed for photoionization and collisional ionization production of OVI, and only one model prediction is shown in Figure 9. Higher-resolution OVI data would be needed to distinguish between photoionization and collisional ionization of the phase of gas that gives rise to the OVI absorption in system C.

Higher-resolution coverage of OVI for the absorption systems at  $z \sim 0.93$  is important to test the validity of the modeling techniques we have used here, and to better understand the physical conditions in the gas. However, we also note that the basic conclusions of the present work, with our new STIS/E230M observations, are not substantially different than those that we reached based upon lower-resolution FOS spectra, using Keck/HIRES observations of MgII as a “template”. Therefore, we probably already have a reasonably accurate view of the physical conditions in the gas. What is really needed to interpret this set of absorption systems along the PG 1206 + 459 line of sight, is to place them into the context of a larger, representative sample. It is already apparent that more quasar lines of sight need to be observed in order to fully sample the variety of galaxy morphologies, environments, and local processes that influence the gas.

Support for this work was provided by the NSF (AST 96–17185), and by NASA (NAG 5–6399 and STSI GO–08672.01–A). We thank Buell Jannuzi, Karen Kneirman, and Rajib Ganguly for their assistance with and participation in the CryoCam observations. We also thank Buell Jannuzi for helpful comments on this manuscript. Blair Savage and Todd Tripp provided useful insights that helped us to refine our results. Finally, we thank the staff at the Space Telescope Science Institute, especially Tricia Royle, for their excellent services.

## REFERENCES

- Bahcall, J. N., et al. 1993, *ApJS*, 87, 1
- Bahcall, J. N., et al. 1996, *ApJ*, 457, 19
- Bergeron, J., & Boissé, P. 1991, *A&A*, 243, 344
- Bergeron, J., Cristiani, S., & Shaver, P. A. 1992, *A&A*, 257, 417
- Bergeron, J., et al. 1994, *ApJ*, 436, 33

- Blitz, L. 2002, in *Extragalactic Gas at Low Redshift*, ed. J. S. Mulchaey and J. Stocke (San Francisco: ASP), 215
- Bowen, D. V., Blades, J. C., & Pettini, M. 1995, *ApJ*, 448, 662
- Brown, T. et al. *HST STIS Data Handbook*, version 4.0, ed. Mobasher, Baltimore, STScI
- Bruzual, A. G., & Charlot, S. 1993, *ApJ*, 405, 538
- Charlton, J. C., & Churchill, C. W. 1996, *ApJ*, 465, 631
- Charlton, J. C., & Churchill, C. W. 1998, *ApJ*, 499, 181
- Charlton, J. C., Ding, J., Zonak, S. G., & Churchill, C. W. 2002, *ApJ*, accepted
- Chen, H.-W., Lanzetta, K. M., Webb, J. K. 2001, *ApJ*, 556, 158
- Churchill, C. W. 1997, Ph.D. Thesis, University of California, Santa Cruz
- Churchill, C. W., & Charlton, J. C. 1999, *AJ*, 118, 59
- Churchill, C. W., Charlton, J. C., & Masiero, J. 2002, in *Extragalactic Gas at Low Redshift*, ed. J. S. Mulchaey and J. Stocke, (San Francisco: ASP), 236.
- Churchill, C. W., Mellon, R. R., Charlton, J. C., Jannuzi, B. T., Kirhakos, S., Steidel, C. C., & Schneider, D. P. 1999, *ApJ*, 519, L43
- Churchill, C. W., Mellon, R. R., Charlton, J. C., Jannuzi, B. T., Kirhakos, S., Steidel, C. C., & Schneider, D. P. 2000a, *ApJS*, 130, 91
- Churchill, C. W., Mellon, R. R., Charlton, J. C., Jannuzi, B. T., Kirhakos, S., Steidel, C. C., & Schneider, D. P. 2000b, *ApJ*, 543, 577
- Churchill, C. W., Rigby, J. R., Charlton, J. C., & Vogt, S. S. 1999, *ApJS*, 120, 51
- Churchill, C. W., Steidel, C. S., & Vogt, S. S. 1996, *ApJ*, 471, 164
- Churchill, C. W., & Vogt, S. S. 2001, *AJ*, 122, 679
- Ding, J., Charlton, J. C., Bond, N. A., Zonak, S. G., & Churchill, C. W. 2003, *ApJ*, in press
- Ferland, G. J., Korista, K. T., Verner, D. A., Ferguson, J. W., Kingdon, J. B., & Verner, E. M. 1998, *PASP*, 110, 761
- Ganguly, R., Churchill, C. W., & Charlton, J. C., 1998, *ApJ*, 498, 103

- Haardt, F., and Madau, P. 1996, *ApJ*, 461, 20
- Heiles, C. 1997, *ApJ*, 481, 193
- Hoopes, C. G., Sembach, K. R., Howk, J. C., Savage, B. D., & Fullerton, A. W. 2002, *ApJ*, 569, 233
- Horne, K. 1986, *PASP*, 98, 609
- Howk, J. C., Savage, B. D., Sembach, K. R., & Hoopes, C. G. 2002, *ApJ*, 572, 264
- Hurwitz, M., Jelinsky, P., & Dixon, W. V. D. 1997, *ApJ*, 481, L31
- Jannuzi, B. T., et al. 1998, *ApJS*, 118, 1
- Kirhakos, S., Sargent, W. L. W., Schneider, D. P., Bahcall, J. N., Jannuzi, B. T., Maoz, D., & Small, T. A. 1994, *PASP*, 106, 646
- Lauroesch, J. T., Truran, J. W., Welty, D. E., & York, D. G. 1996, *PASP*, 108, 641
- Le Brun, V., Bergeron, J., Boissé, P., & Christian, C. 1993, *A&A*, 279, 33
- Marsh, T. 1989, *PASP*, 101, 1032
- Mateo, M. 1998, *ARAA*, 36, 435
- Oegerle, W. R., Tripp, T. M., Sembach, K. R., Jenkins, E. B., Bowen, D. V., Cowie, L. L., Green, R. F., Kruk, J. W., Savage, B. D., Shull, J. M., & York, D. G. 2000, *ApJ*, 538, L23
- Putman, M. E. 2002, *AJ*, 123, 873
- Rigby, J. R., Charlton, J. C., & Churchill, C. W. 2002, *ApJ*, 565, 743
- Savage, B. D., & Sembach, K. R. 1991, *ApJ*, 379, 245
- Savage, B. D., Sembach, K. R., & Lu, L. 1994, *ApJ*, 420, 183
- Savage, B. D., Sembach, K. R., & Lu, L. 1995, *ApJ*, 449, 145
- Savage, B. D., Sembach, K. R., & Lu, L. 1997, *AJ*, 113, 2158
- Schechter, P., 1976, *ApJ*, 203, 297
- Schneider, D. P., et al. 1993, *ApJS*, 87, 45

- Sembach, K. R., Savage, B. D., Lu, L., & Murphy, E. M. 1999, *ApJ*, 515, 108
- Slavin, J. D., & Cox, D. P. 1992, *ApJ*, 392, 131
- Slavin, J. D., & Cox, D. P. 1993, *ApJ*, 417, 187
- Steidel, C. C. 1995, in *QSO Absorption Lines*, ed. G. Meylan (New York: Springer), 139
- Steidel, C. C., in *Galactic Halos*, ed. D. Zaritsky (San Francisco: ASP), 167.
- Steidel, C. C., Dickinson, M., Meyer, D. M., Adelberger, K. L., & Sembach, K. R. 1997, *ApJ*, 480, 568
- Steidel, C. C., Dickinson, M. & Persson, E. 1994, *ApJ*, 437, L75
- Steidel, C. C., Kollmeier, J. A., Shapley, A. E., Churchill, C. W., Dickinson, M. & Pettini, M. 2002, *ApJ*, 570, 526
- Sutherland, R. S. & Dopita, M. A. 1993, *ApJS*, 88, 253
- Thimm, G. 1995, in *QSO Absorption Lines*, ed. G. Meylan (New York: Springer), 169
- Tripp, T. M., Girous, M. L., Stocke, J. T., Tumlinson, J., & Oegerle, W. R. 2001, *ApJ*, 563, 724
- Vogt, S. S. et al. 1994, *Proc. SPIE*, 2198, 362
- Wakker, B. P., and van Woerden, H. 1997, *ARA&A*, 35, 509
- Zonak, S. G., Charlton, J. C., Ding, J., & Churchill, C. W. 2003, *ApJ*, submitted

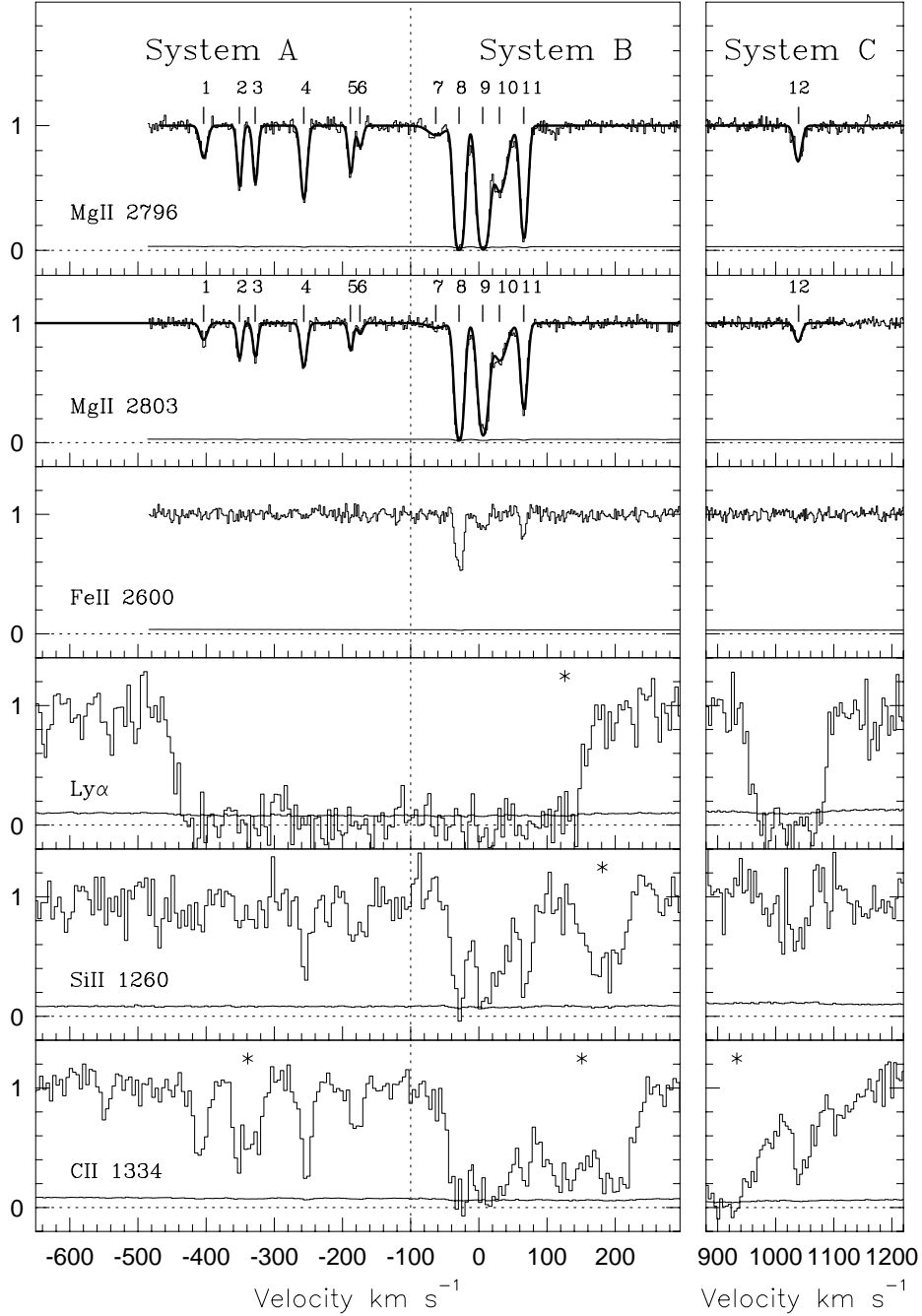


Fig. 1.— The spectra of various transitions are displayed as histograms in velocity space in the figure above. The MgII and FeII profiles are covered by HIRES/Keck ( $R = 45,000$ ), while the others are STIS/*HST* ( $R = 30,000$ ) data. The spectra are normalized in velocity space, with zero-point at  $z = 0.9276$ . A  $1\sigma$  level error is indicated by the line at the bottom of each spectrum. The “\*” above the continuum indicates that the spectrum is contaminated by a known blend at that location (see § 3.1.2). The solid lines superimposed on the MgII spectrum are the Voigt profile fit. The vertical ticks above the fit label the locations of the individual MgII clouds obtained from the Voigt profile fit. The designated cloud numbers are consistent with the ones listed in Tables 3–5.

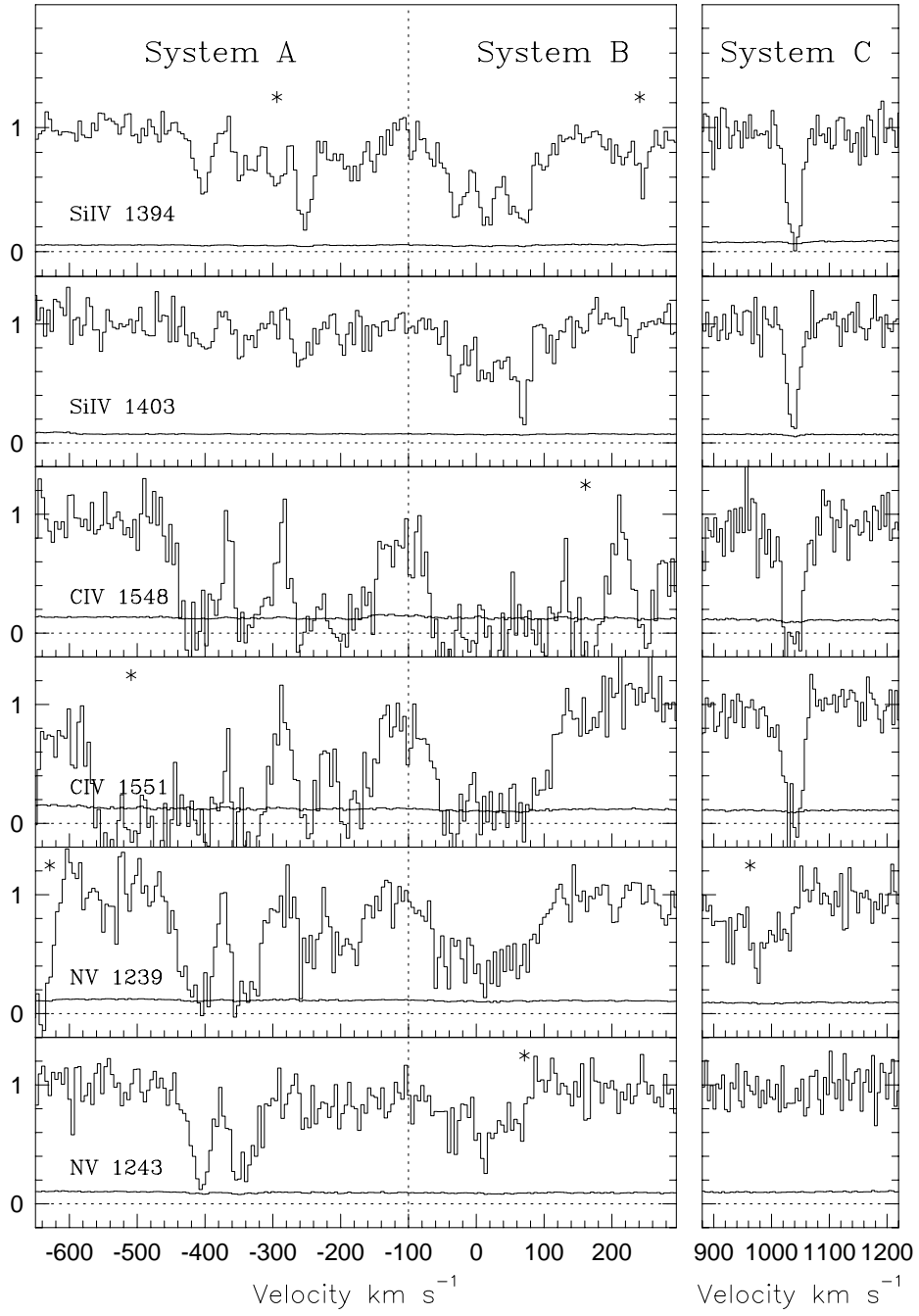


Fig. 2.— Same as Figure 1, but for the high-ionization transitions.



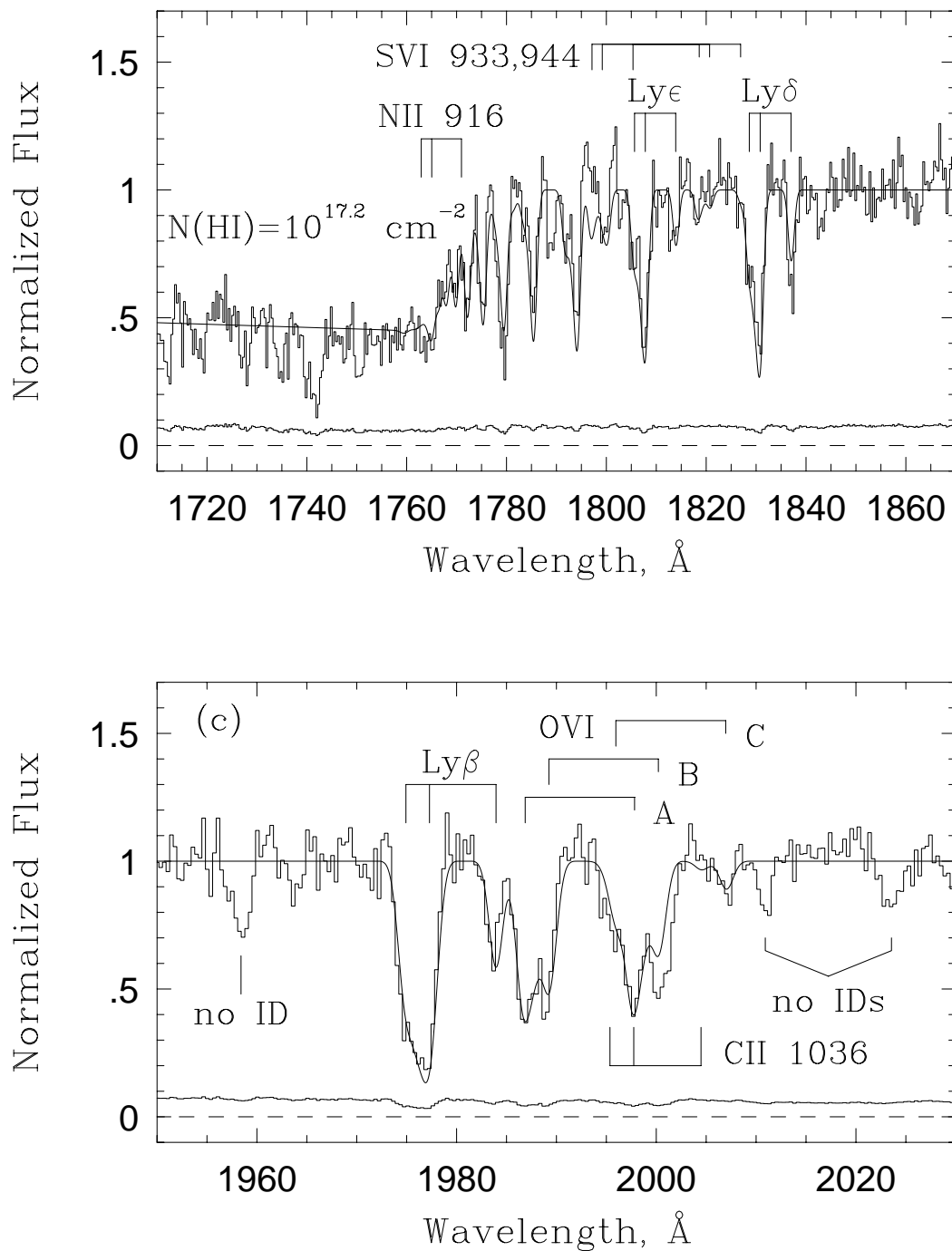


Fig. 3.— A partial Lyman limit break, covered by the FOS spectrum, is displayed in wavelength space above. The higher order Lyman series and the OVI profiles are also shown. An example of an acceptable model for the three systems (the solid curve) is superimposed on the data (histogram). The parameters of this model are listed in Tables 3–5.

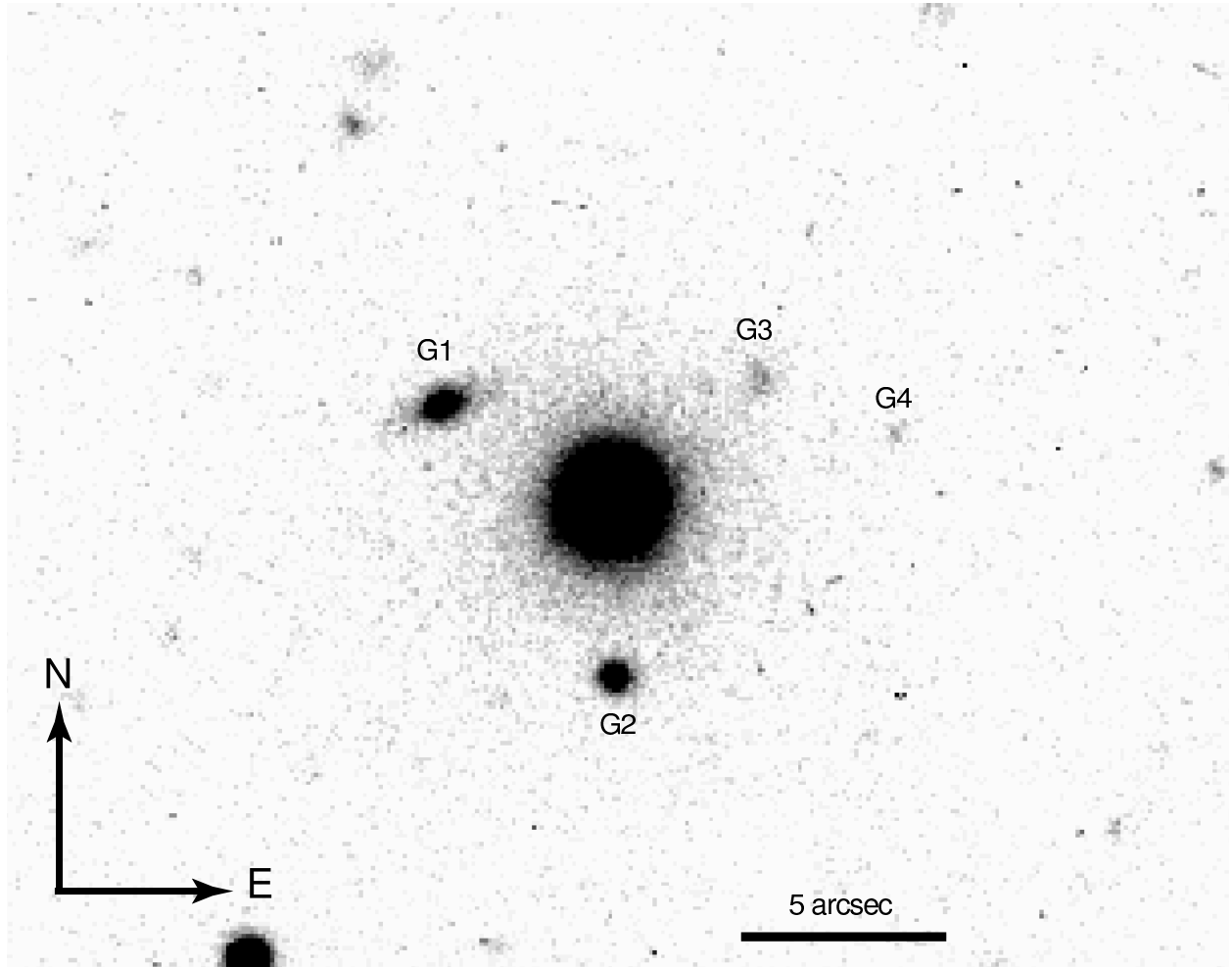


Fig. 4.— The WIYN image of the quasar PG 1206 + 459 field is shown above. The bright, central object is the quasar. Four galaxies, G1, G2, G3, and G4, are detected in the field. G2 has a detected [OII]  $\lambda 3727$  emission line in its long-slit spectrum. G3 is marginally detected in a Fabry–Perot image, tuned to the redshifted [OII]  $\lambda 3727$  line (Thimm 1995).

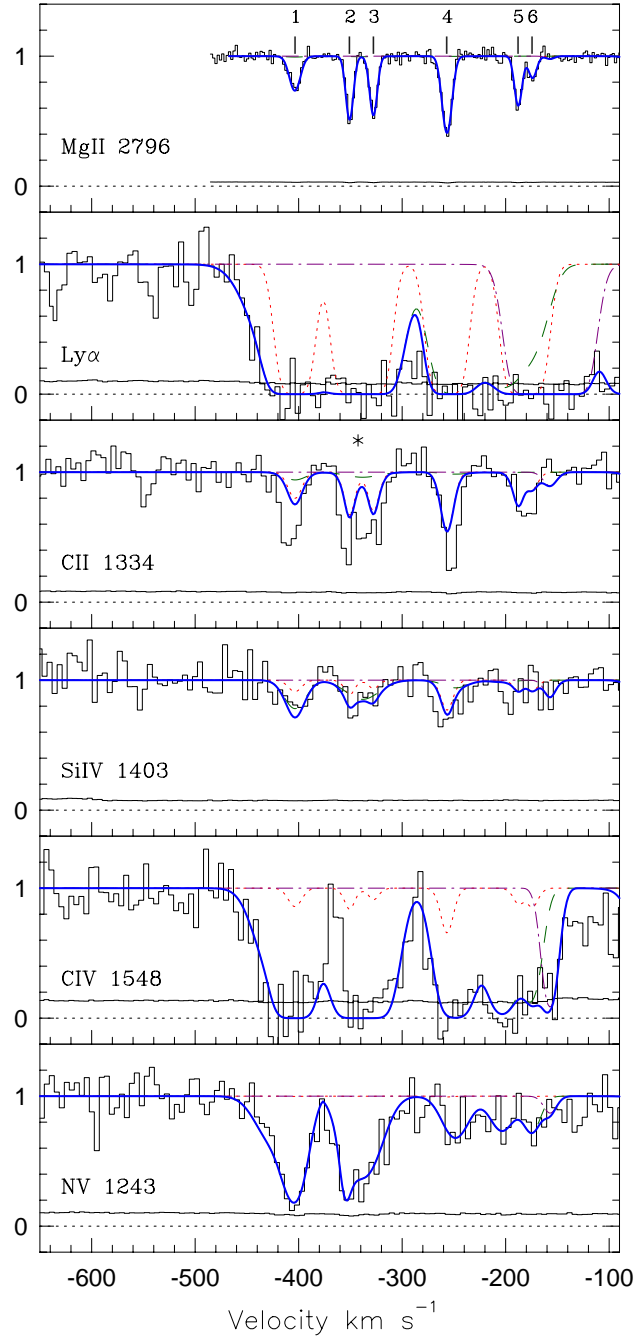


Fig. 5.— System A ( $z = 0.9254$ ) spectra are shown in the figure above, with model curves superimposed. The model parameters for this system are given in Table 3. The histograms, vertical ticks, and asterisks are as indicated in the caption of Figure 1. The dotted lines represent contributions from our model of the MgII clouds. The dashed curves show the contributions from the photoionized, diffuse phase. The dashed-dotted lines represent the intermediate, photoionized component. The thick, solid curve shows the contribution from all phases, which also includes blended contributions from all three systems.

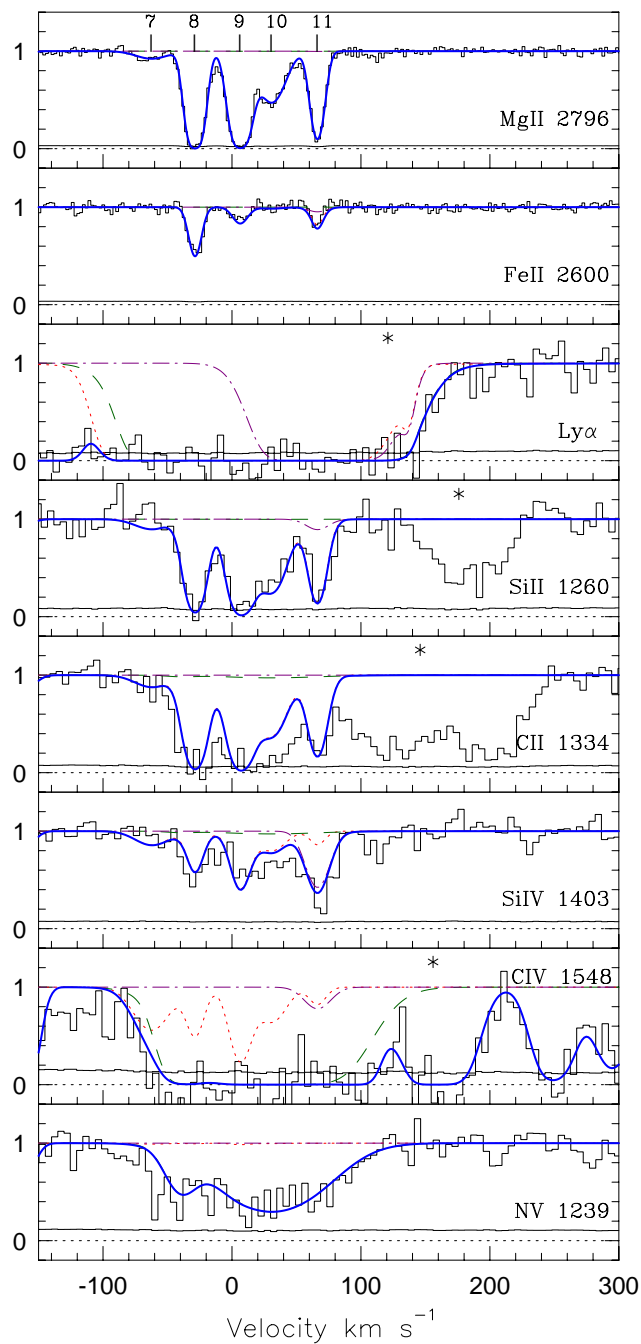


Fig. 6.— System B ( $z = 0.9276$ ) spectra are shown, with model curves superimposed. The model parameters for this system are given in Table 4. The histograms, vertical ticks, and asterisks are as indicated in the caption of Figure 1. Model curves represent the different phases of gas, as outlined in the caption to Figure 5.

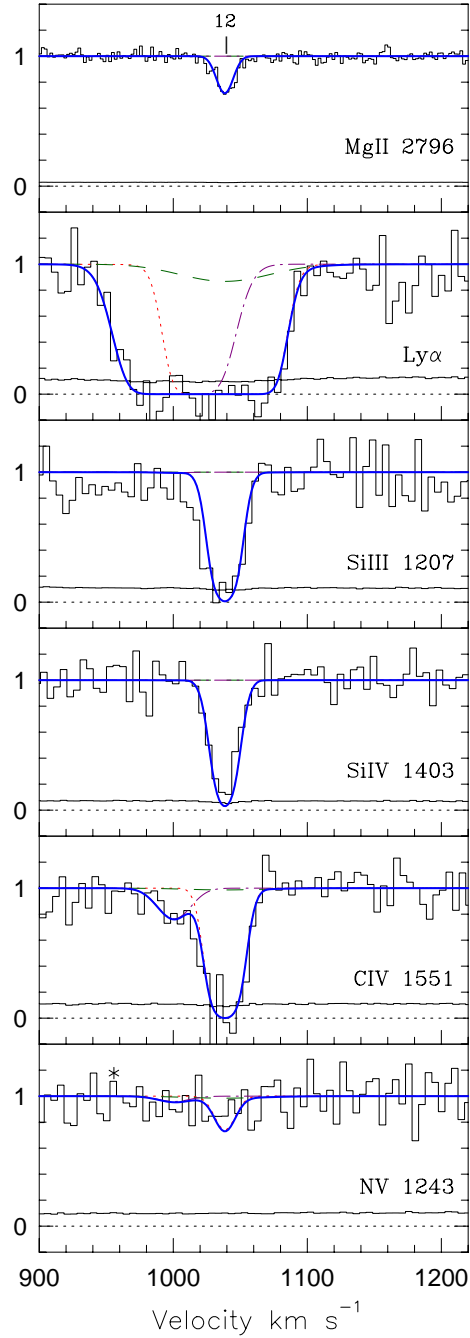


Fig. 7.— System C ( $z = 0.9342$ ) spectra are shown, with model curves superimposed. The model parameters for this system are given in Table 5. The different curves denote separate model phases as described in the caption to Figure 5.

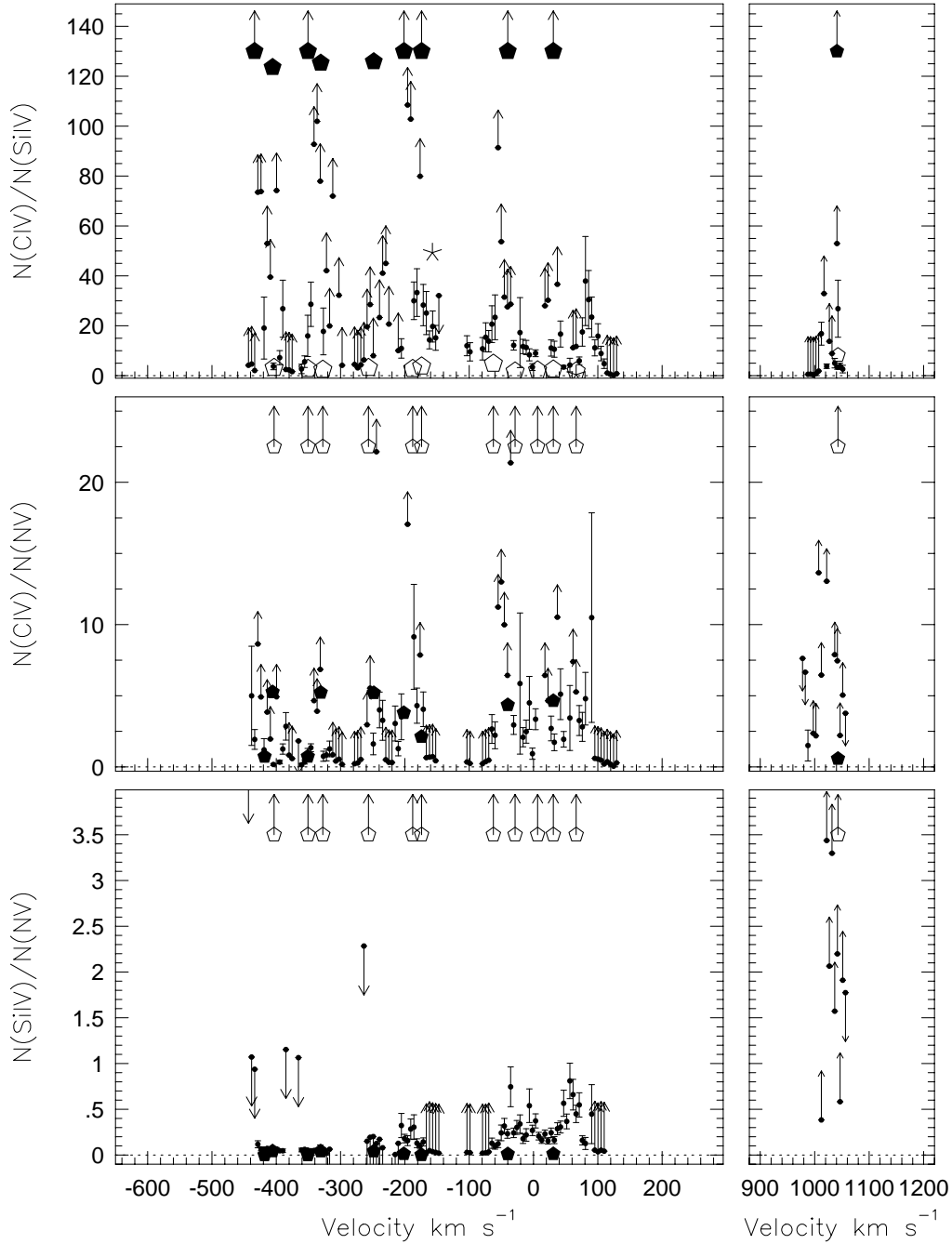


Fig. 8.— The ratios of apparent column density between SiIV, CIV, and NV are displayed for all three systems in velocity space above. The small dots represent the unsaturated *HST*/STIS data, with  $1\sigma$  errors superimposed. The upper/lower data limits are denoted by small dots with upper/lower arrows superimposed. The open pentagons represent the model values for our low-ionization clouds, the filled pentagons show the contribution from the diffuse phase, and the skeletal point represents the intermediate component. The pentagons with upper arrows superimposed indicate that the actual ratios are too large to be displayed on the plots.

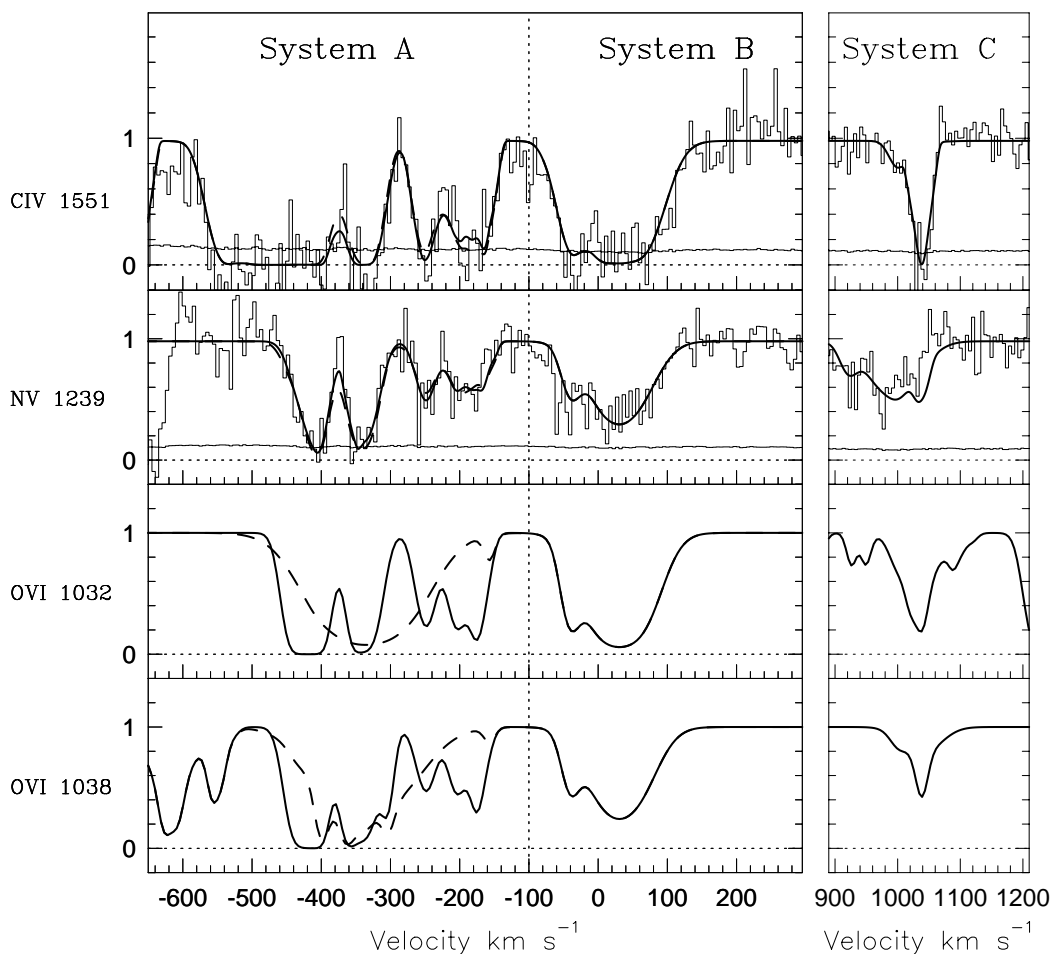


Fig. 9.— Simulated models of OVI  $\lambda\lambda 1032, 1038$  as it would be observed by the *HST*/COS ( $R = 18,000$ ) are displayed above as solid curves. The simulations use the model parameters listed in Table 3–5, with a photoionized component in the diffuse phase of system C. Solid curves are for the photoionization model for system A, and dashed lines for the collisional ionization model. The CIV and NV profiles are also displayed for comparison. The synthetic model curves are superimposed on the STIS data covering these two transitions.

Table 1. Rest Frame Equivalent Widths

	System A $z = 0.92540$	System B $z = 0.92760$	System C $z = 0.93428$
Ly $\alpha$	$< 2.38 \pm 0.03$	$< 2.38 \pm 0.03$	$0.55 \pm 0.02$
MgI $\lambda 2853$	$< 0.006$	$0.04 \pm 0.02$	$< 0.006$
MgII $\lambda 2796$	$0.22 \pm 0.02$	$0.66 \pm 0.01$	$0.05 \pm 0.01$
MgII $\lambda 2803$	$0.12 \pm 0.02$	$0.51 \pm 0.01$	$0.02 \pm 0.01$
FeII $\lambda 2600$	$< 0.006$	$0.08 \pm 0.02$	$< 0.006$
SiII $\lambda 1260$	$0.16 \pm 0.03$	$0.34 \pm 0.02$	$0.16 \pm 0.01$
CII $\lambda 1335$	$< 0.25 \pm 0.03$	$0.94 \pm 0.02$	$0.10 \pm 0.01$
SiIII $\lambda 1207$	$0.78 \pm 0.09$	$0.66 \pm 0.02$	$0.14 \pm 0.02$
SiIV $\lambda 1394$	$< 0.41 \pm 0.02$	$0.46 \pm 0.01$	$0.10 \pm 0.01$
SiIV $\lambda 1403$	$0.10 \pm 0.02$	$0.28 \pm 0.02$	$0.11 \pm 0.01$
CIV $\lambda 1548$	$1.28 \pm 0.08$	$1.98 \pm 0.20$	$0.31 \pm 0.02$
CIV $\lambda 1551$	$1.98 \pm 0.20$	$0.91 \pm 0.07$	$0.22 \pm 0.02$
NV $\lambda 1239$	$0.76 \pm 0.06$	$0.28 \pm 0.02$	$< 0.02$
NV $\lambda 1243$	$0.28 \pm 0.02$	$0.21 \pm 0.02$	$< 0.02$

Note. — Upper limits for non-detections are at a  $3\sigma$  level. Upper limits with specified error bars are from blends that could not be distinctly separated by Gaussian fits.



Table 2. Galaxy Properties

	luminosity [ $L_K^*$ ]	Impact Parameter [ $h^{-1} kpc$ ]	redshift
G1	2	43	...
G2	1	38	0.9289
G3	0.2	43	$\sim 0.93$
G4	0.1	65	...

Note. — The impact parameters are calculated assuming  $z \sim 0.93$ .

Table 3. System A at  $z = 0.9254$ 

	$v$ [km s <sup>-1</sup> ]	$Z$ [ $Z_{\odot}$ ]	$\log U$	$\log n_H$ [cm <sup>-3</sup> ]	size [kpc]	$T$ [K]	$N_{\text{tot}}(\text{H})$ [cm <sup>-2</sup> ]	$N(\text{H I})$ [cm <sup>-2</sup> ]	$N(\text{Mg II})$ [cm <sup>-2</sup> ]	$N(\text{Si IV})$ [cm <sup>-2</sup> ]	$N(\text{C IV})$ [cm <sup>-2</sup> ]	$N(\text{N V})$ [cm <sup>-2</sup> ]	$b(\text{H})$ [km s <sup>-1</sup> ]	$b(\text{Mg})$ [km s <sup>-1</sup> ]	$b(\text{N})$ [km s <sup>-1</sup> ]
Mg II PHASE															
Mg II-1	-403	3	-2.6	-2.6	0.007	2300	16.8	14.7	11.9	12.2	12.5	11.1	10.5	6.0	6.2
Mg II-2	-351	3	-2.7	-2.5	0.008	2200	16.9	14.9	12.2	12.2	12.5	11.1	8.9	2.9	3.3
Mg II-3	-328	3	-2.8	-2.4	0.005	2200	16.8	14.9	12.1	12.0	12.2	10.7	9.0	3.0	3.3
Mg II-4	-257	3	-2.6	-2.6	0.02	2300	17.2	15.1	12.4	12.6	12.9	11.5	9.8	4.8	5.0
Mg II-5	-188	3	-2.7	-2.5	0.006	2200	16.7	14.8	12.0	12.1	12.3	10.9	9.0	3.1	3.4
Mg II-6	-174	3	-2.5	-2.7	0.006	2500	16.6	14.4	11.6	12.1	12.4	11.1	9.6	3.7	4.0
INTERMEDIATE PHASE															
C IV-ph	-157	0.1	-2.0	-3.2	5	12000	17.9	15.6	10.7	12.3	14.0	12.9	19.8	4.4	5.6
C IV-co	-157	0.01	...	...	...	100000	20.0	15.2	9.4	12.2	14.0	11.2	4.2	5.8	5.6
	$v$ [km s <sup>-1</sup> ]	$Z$ [ $Z_{\odot}$ ]	$\log U$	$\log n_H$ [cm <sup>-3</sup> ]	size [kpc]	$T$ [K]	$N_{\text{tot}}(\text{H})$ [cm <sup>-2</sup> ]	$N(\text{H I})$ [cm <sup>-2</sup> ]	$N(\text{O VI})$ [cm <sup>-2</sup> ]	$N(\text{Si IV})$ [cm <sup>-2</sup> ]	$N(\text{C IV})$ [cm <sup>-2</sup> ]	$N(\text{N V})$ [cm <sup>-2</sup> ]	$b(\text{H})$ [km s <sup>-1</sup> ]	$b(\text{O})$ [km s <sup>-1</sup> ]	$b(\text{N})$ [km s <sup>-1</sup> ]
DIFFUSE PHASE (CASE A: PHOTOIONIZATION)															
N V-1	-424	3	-0.6	-4.6	31	25000	18.4	13.6	15.1	8.1	13.7	13.8	28.7	21.0	21.1
N V-2	-403	3	-1.5	-3.7	3	8000	18.3	14.8	14.7	12.8	14.9	14.2	16.6	12.6	12.6
N V-3	-355	3	-0.6	-4.6	65	25000	18.7	13.9	15.4	8.4	14.0	14.2	10.9	2.7	2.9
N V-4	-338	3	-1.5	-3.7	3	8000	18.3	14.8	14.7	12.8	14.9	14.2	23.7	21.1	21.1
N V-5	-248	3	-1.5	-3.7	1	8000	17.4	14.3	14.1	12.3	14.4	13.7	19.1	15.7	15.7
N V-6	-204	3	-1.4	-3.8	1	10000	17.8	13.9	14.1	11.6	14.1	13.5	18.7	14.0	14.1
N V-7	-175	3	-1.2	-4.0	1	15000	17.6	13.4	14.2	10.5	13.7	13.4	17.5	9.0	9.1
DIFFUSE PHASE (CASE B: COLLISIONAL IONIZATION)															
N V-1	-418	3	...	...	...	150000	18.0	12.8	11.9	11.8	13.7	13.6	52.7	20.1	21.3
N V-2	-406	3	...	...	...	150000	18.8	13.6	12.6	12.6	14.4	14.3	50.5	14.2	15
N V-3	-351	3	...	...	...	150000	18.5	13.2	12.3	12.3	14.1	14.0	50.8	15.3	16
N V-4	-331	3	...	...	...	140000	18.7	13.6	11.9	12.7	14.6	14.0	48.7	15.4	16
N V-5	-248	3	...	...	...	140000	18.3	13.2	11.4	12.3	14.2	13.6	49.0	16.2	16.8
N V-6	-202	3	...	...	...	140000	18.3	13.2	11.5	12.2	14.2	13.6	48.8	15.7	16.3
N V-7	-174	3	...	...	...	140000	18.1	13.0	11.2	12.0	14.0	13.4	48.4	14.3	15
O VI-ph	-335	3	-0.6	-4.6	31	250000	18.4	13.6	15.0	7.92	13.6	13.7	82.4	80.0	80.0
O VI-co	-335	3	...	...	...	320000	18.5	12.6	15.0	11.1	12.7	13.1	106	80.0	80.3

Note. — Column densities are listed in logarithmic units. In the intermediate-ionization phase, both the photoionization and the collisional ionization cases are listed. In Case B for the diffuse phase, there is a collisionally ionized N V accompanied by either the photoionized or the collisionally ionized O VI cloud listed directly below.

Table 4. System B at  $z = 0.9276$ 

	$v$ [km s <sup>-1</sup> ]	$Z$ [ $Z_{\odot}$ ]	$\log U$	$\log n_H$ [cm <sup>-3</sup> ]	size [kpc]	$T$ [K]	$N_{\text{tot}}(\text{H})$ [cm <sup>-2</sup> ]	$N(\text{H I})$ [cm <sup>-2</sup> ]	$N(\text{Mg II})$ [cm <sup>-2</sup> ]	$N(\text{Si IV})$ [cm <sup>-2</sup> ]	$N(\text{C IV})$ [cm <sup>-2</sup> ]	$N(\text{N V})$ [cm <sup>-2</sup> ]	$b(\text{H})$ [km s <sup>-1</sup> ]	$b(\text{Mg})$ [km s <sup>-1</sup> ]	$b(\text{N})$ [km s <sup>-1</sup> ]
Mg II PHASE															
Mg II-7	-62	1.0	-2.5	-2.7	0.1	10000	17.7	15.1	11.7	12.7	13.4	11.8	24.5	16.2	16.5
Mg II-8	-29	1.0	-3.2	-2	0.1	8000	18.6	16.7	13.4	13.0	13.2	11.3	17.3	5.7	6.4
Mg II-9	6	1.0	-3.0	-2.2	0.2	9000	18.6	16.5	13.3	13.2	13.6	11.7	18.3	7.4	8.0
Mg II-10	31	1.0	-2.9	-2.3	0.1	9000	18.0	15.8	12.6	12.8	13.2	11.4	21.3	12.7	13.1
Mg II-11	66	1.0	-3.2	-2	0.03	8500	18.0	16.1	12.8	12.4	12.6	10.7	17.4	5.1	5.9
INTERMEDIATE PHASE															
Si IV-ph	66	0.25	-2.5	-2.7	2	16000	19.0	16.2	12.3	13.3	14.1	12.5	18.8	10.0	10.5
Si IV-co	66	0.25	...	...	...	63000	18.8	14.7	10.0	13.3	12.9	7.6	33	10.3	11.7
	$v$ [km s <sup>-1</sup> ]	$Z$ [ $Z_{\odot}$ ]	$\log U$	$\log n_H$ [cm <sup>-3</sup> ]	size [kpc]	$T$ [K]	$N_{\text{tot}}(\text{H})$ [cm <sup>-2</sup> ]	$N(\text{H I})$ [cm <sup>-2</sup> ]	$N(\text{O VI})$ [cm <sup>-2</sup> ]	$N(\text{Si IV})$ [cm <sup>-2</sup> ]	$N(\text{C IV})$ [cm <sup>-2</sup> ]	$N(\text{N V})$ [cm <sup>-2</sup> ]	$b(\text{H})$ [km s <sup>-1</sup> ]	$b(\text{O})$ [km s <sup>-1</sup> ]	$b(\text{N})$ [km s <sup>-1</sup> ]
DIFFUSE PHASE															
C IV-8	-40	0.25	-1.6	-3.6	8	23000	18.8	15.0	14.0	11.5	14.1	13.5	23	13.7	13.8
N V-9	31	0.25	-1.6	-3.6	54	22000	19.6	15.8	14.8	12.4	15.0	14.3	53	50.0	50

Note. — Column densities are listed in logarithmic units. In the intermediate-ionization phase, both the photoionization and the collisional ionization cases are listed.

Table 5. System C at  $z = 0.9343$

	$v$ [km s <sup>-1</sup> ]	$Z$ [ $Z_{\odot}$ ]	$\log U$	$\log n_H$ [cm <sup>-3</sup> ]	size [kpc]	$T$ [K]	$N_{\text{tot}}(\text{H})$ [cm <sup>-2</sup> ]	$N(\text{H I})$ [cm <sup>-2</sup> ]	$N(\text{Mg II})$ [cm <sup>-2</sup> ]	$N(\text{Si IV})$ [cm <sup>-2</sup> ]	$N(\text{C IV})$ [cm <sup>-2</sup> ]	$N(\text{N V})$ [cm <sup>-2</sup> ]	$b(\text{H})$ [km s <sup>-1</sup> ]	$b(\text{Mg})$ [km s <sup>-1</sup> ]	$b(\text{N})$ [km s <sup>-1</sup> ]
Mg II PHASE															
Mg II-12	1042	1.25	-2.0	-3.2	4	10000	18.9	15.7	12.1	14.1	15.0	13.4	20	7.5	8.2
OFFSET PHASE															
C IV-off	1005	0.063	-1.6	-3.6	6	30000	16.6	14.8	8.4	10.5	13.3	12.7	26.3	14.8	15.3
	$v$ [km s <sup>-1</sup> ]	$Z$ [ $Z_{\odot}$ ]	$\log U$	$\log n_H$ [cm <sup>-3</sup> ]	size [kpc]	$T$ [K]	$N_{\text{tot}}(\text{H})$ [cm <sup>-2</sup> ]	$N(\text{H I})$ [cm <sup>-2</sup> ]	$N(\text{O VI})$ [cm <sup>-2</sup> ]	$N(\text{Si IV})$ [cm <sup>-2</sup> ]	$N(\text{C IV})$ [cm <sup>-2</sup> ]	$N(\text{N V})$ [cm <sup>-2</sup> ]	$b(\text{H})$ [km s <sup>-1</sup> ]	$b(\text{O})$ [km s <sup>-1</sup> ]	$b(\text{N})$ [km s <sup>-1</sup> ]
DIFFUSE PHASE															
O VI-ph	1042	1.0	-0.5	-4.7	13	31000	17.9	12.9	14.0	7.6	6.1	12.6	45.6	40.0	40.1
O VI-co	1042	1.0	...	...	...	320000	17.9	12.0	14.0	10.1	11.7	12.1	80.6	40.0	40.6

Note. — Column densities are listed in logarithmic units. For cloud Mg II-12, the abundance of silicon was increased by 0.4 dex, and the abundance of nitrogen was decreased by 0.4 dex. For the high-ionization phase, both the photoionization and the collisional ionization cases are listed.